Journal of proteome research

pubs.acs.org/jpr

Article

Comprehensive Examination of the Mouse Lung Metabolome Following *Mycobacterium tuberculosis* Infection Using a Multiplatform Mass Spectrometry Approach

Miguel Fernández-García, Fernanda Rey-Stolle, Julien Boccard, Vineel P. Reddy, Antonia García, Bridgette M. Cumming, Adrie J. C. Steyn, Serge Rudaz, and Coral Barbas*

Cite This: *J. Proteome Res.* 2020, 19, 2053−2070

Read Online

ACCESS | Metrics & More | Article Recommendations | Supporting Information

ABSTRACT: The mechanisms whereby *Mycobacterium tuberculosis* (*Mtb*) rewires the host metabolism in vivo are surprisingly unexplored. Here, we used three high-resolution mass spectrometry platforms to track altered lung metabolic changes associated with *Mtb* infection of mice. The multiplatform data sets were merged using consensus orthogonal partial least squares-discriminant analysis (cOPLS-DA), an algorithm that allows for the joint interpretation of the results from a single multivariate analysis. We show that *Mtb* infection triggers a temporal and progressive catabolic state to satisfy the continuously changing energy demand to control infection. This causes dysregulation of metabolic and oxido-reductive pathways culminating in *Mtb*-associated wasting. Notably, high abundances of trimethylamine-*N*-oxide (TMAO), produced by the host from the bacterial metabolite trimethylamine upon infection, suggest that *Mtb* could exploit TMAO as an electron acceptor under anaerobic conditions. Overall, these new pathway alterations advance our understanding of the link between *Mtb* pathogenesis and metabolic dysregulation and could serve as a foundation for new therapeutic intervention strategies. Mass spectrometry data has been deposited in the Metabolomics Workbench repository (data-set identifier: ST001328).

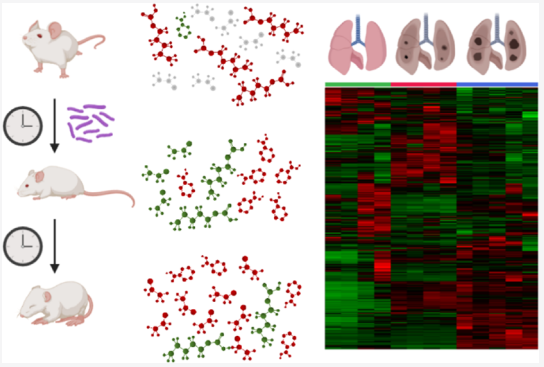

KEYWORDS: *tuberculosis, metabolomics, pulmonary tuberculosis, tuberculosis progression, functional metabolomics, multiplatform metabolomics, data fusion*

INTRODUCTION

Tuberculosis (TB) is caused by the obligate pathogen *Mycobacterium tuberculosis* (*Mtb*). It is estimated that one-quarter of the world's population is latently infected with the bacilli, from which 5−10% develop active tuberculosis.[1,2] The increased prevalence of multidrug-resistant TB (MDR-TB) and extensively drug-resistant TB (XDR-TB) cases represents a potential threat to global health as the therapeutic arsenal for drug-resistant TB treatment is limited.[3] Thus, there is an urgent need for new diagnostic and therapeutic strategies to control this epidemic, including new biomarkers and host-directed therapies, the development of which would be assisted by a comprehensive mechanistic knowledge of host−pathogen interactions.

Metabolomics has been employed for the identification of TB diagnostic biomarkers, the evaluation of potential therapeutics, and the study of the biological mechanisms underlying TB disease onset and progression in both in vitro and in vivo animal models, as well as in human patients.[4−6] Characterizing how the host metabolome is altered during *Mtb* infection is critically important as it may lead to the discovery of new pathways essential for protection against the bacillus and the identification of host-directed therapies.

Previous metabolomic studies in the TB field have contributed to our knowledge of the in vivo carbon sources available to *Mtb*,[7,8] the ability of *Mtb* to withstand the oxido-reductive stress present in the TB lung,[9] and the role of immunometabolism in driving effector functions of the immune cells in tuberculosis.[10−14] However, there is a gap in our understanding of how *Mtb* infection modulates the host metabolome over the course of infection; several reasons are responsible for this breach in our knowledge. First, a limiting factor is that few studies have examined the dynamic metabolic alterations that occur during the course of *Mtb* infection.[15] For example, only three metabolomic studies using nuclear magnetic resonance (NMR) examined the lungs of *Mtb*-infected animal

Received: December 31, 2019
Published: April 14, 2020

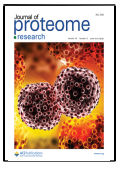

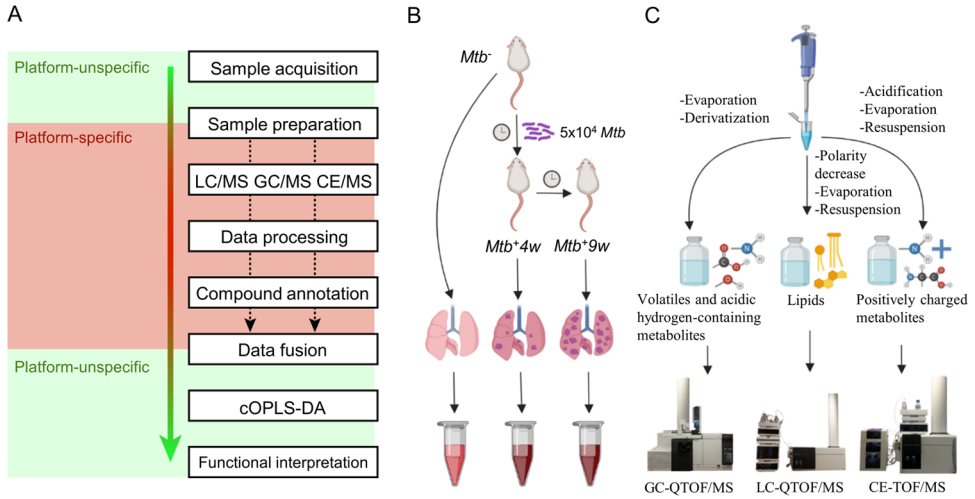

Figure 1. Applied metabolomic workflow summary. Simplified metabolomic workflow (A), including consensus orthogonal partial least squares discriminant analysis (cOPLS-DA) data fusion approach. Experimental design, and lung homogenate collection (B). Platform-specific sample treatment and HRMS analysis (C). "Platform unspecific" refers to tasks that are universal regardless of the MS platform being used. "Platform-specific" tasks will vary depending on the MS platform. Note that each metabolomic experiment allows the detection of specific subsets of metabolites.

models,[16−18] of which only one guinea pig pulmonary TB model was investigated at multiple time points.[17,18] While NMR is robust and well established, it suffers from relatively low sensitivity. Second, another limiting factor is that a single platform metabolomic approach was utilized in all lung metabolomic studies.[16−18] The simultaneous use of distinct separation techniques coupled with high-resolution mass spectrometry (HRMS) analyzers enables the separation of specific metabolite subsets according to specific physicochemical properties while permitting accurate mass measurements of the metabolites. Such a multiplatform metabolomic approach can reach higher levels of metabolite coverage, sensitivity, and specificity.[19] Unfortunately, to the best of our knowledge, untargeted multiplatform-based metabolomic analyses to examine how *Mtb* infection affects the lung metabolome have not yet been reported. Likely reasons include the different methodological limitations described for lung metabolomics.[4]

Here, we examined how *Mtb* affects the host metabolome during infection by exploiting capillary electrophoresis-time-of-flight (CE-TOF/MS), gas chromatography-quadrupole-time-of-flight (GC-QTOF/MS), and liquid chromatography-quadrupole-time-of-flight (LC-QTOF/MS) as analytical platforms. A downstream bioinformatics pipeline employing data fusion algorithms, multivariate statistics, and functional metabolomics was then used to characterize the global metabolomic changes in the lungs of *Mtb*-infected mice at different time points during infection (Figure 1A−C). This enabled us to identify new and unexpected host disease-associated metabolic pathways including, but not limited to, amino acid, carbohydrate, and fatty acid metabolism and consumption, central carbon metabolism, oxido-reductive stress, and polyamine metabolism of TB modulated by *Mtb*. Overall, our findings have implications that may contribute toward a better understanding of the mechanisms of the disease and new strategies for the pharmacological control of TB. To the best of our knowledge, this is the first untargeted, MS-based lung metabolomic study characterizing the progression of pulmonary TB in the mouse model for TB.

EXPERIMENTAL SECTION

Mice and *Mtb* Infection

Both male and female age-matched C57BL/6 mice (8−10 weeks old) were infected with *Mtb* H37Rv in an animal BSL-3 laboratory and monitored with food and water ad libitum. Mice were sacrificed by anesthesia with isoflurane followed by gentle cervical dislocation as approved by the institutional Animal Protocol Number (APN): 08591. Mice experimental procedures were approved by the Institutional Animal Care and Use Committee (IACUC) at the University of Alabama at Birmingham. For mice studies, we adhered to the national/international regulation of "Public Health Service Policy on Humane Care and Use of Laboratory Animals" (NIH) and "Animal Welfare Act and Animal Welfare Regulations" (USDA). Mouse genotype was confirmed by PCR and Western blotting. *Mtb* H37Rv was grown at 37 °C with shaking in BD Difco Middlebrook 7H9 media supplemented with 0.2% glycerol and ADS (albumin, dextrose, NaCl) with 0.02% tyloxapol. Mice were infected with 5×10^4 *Mtb* H37Rv via the intratracheal route. Lungs were collected from uninfected (male, $n = 2$; female, $n = 2$) and *Mtb*-infected mice at 4 weeks (male, $n = 2$; female, $n = 2$) and 9 weeks (male, $n = 2$; female, $n = 3$) postinfection and stored immediately at −80 °C for further processing and metabolite extraction.

Metabolite Extraction

Samples for metabolite analysis were prepared as described previously.[11,20] Briefly, 1 mL of 50% methanol was added to 100 mg of *Mtb*-infected or uninfected lung tissue and homogenized in a dounce homogenizer to prepare a uniform suspension. For CE-TOF/MS, 200 μL of homogenate was mixed with 200 μL of 0.2 M formic acid and vortexed for 2 min. The samples were cleared by centrifugation at 16 000*g* for 10 min at 4 °C, and the supernatant was filter-sterilized using 0.22 μm spin-X columns (Sigma). For GC-QTOF/MS and LC-QTOF/MS, 200 μL of each sample homogenate was mixed with 800 μL of 80:20 methanol/methyl *tert*-butyl ether (MTBE) and vortexed for 2 min. Metabolites were then extracted for 1 h with shaking at room temperature and then centrifuged at 4000*g* at 20 °C for 20 min. Supernatants were sterile-filtered using 0.22 μm spin-X

https://dx.doi.org/10.1021/acs.jproteome.9b00868
J. Proteome Res. 2020, 19, 2053−2070

columns. All samples were passed through a Millipore filter (30 kDa cutoff) to remove large proteins. Samples were dried under high vacuum and stored at −80 °C until further platform-specific processing and analysis.

CE-TOF/MS Analysis

The dried samples were resuspended in Milli-Q water containing 0.1 mM formic acid and 0.2 mM methionine sulfone (internal standard) (Sigma-Aldrich, Germany) by vortexing for 1 min. After subsequent centrifugation (12 600*g*, 15 min), the resulting clear solution was analyzed by CE-TOF/MS using a CE system (Agilent 7100) coupled to a TOF/MS system (Agilent 6224). The separation occurred in a fused-silica capillary (Agilent Technologies) (total length, 96 cm; i.d., 50 μm) under normal polarity with a background electrolyte containing 1.0 M formic acid in 10% (v/v) methanol at 20 °C. Sheath liquid (6 μL·min^{-1}) was methanol/water (1:1, v/v) containing 1.0 mM formic acid with two reference masses to allow correction and high mass resolution in the MS. Samples were hydrodynamically injected at 50 mbar for 35 s and stacked by injecting a background electrolyte at 100 mbar for 10 s. The optimized MS parameters were as follows: fragmentor, 125 V; skimmer, 65 V; octopole, 750 V; nebulizer pressure, 10 psi; drying gas temperature, 200 °C; and flow rate, 10.0 L·min^{-1}. The capillary voltage was 3500 V. Data were acquired in the positive electrospray ionization (ESI) mode with a full scan from m/z 50 to 1000 at a rate of 1 spectra·s^{-1}. The resulting CE-TOF/MS data files were cleaned of background noise and unrelated ions by the Batch Recursive Feature Extraction tool with Agilent MassHunter Profinder version B.06.00 software. Data were extracted using a data-mining algorithm based on the software. To perform an initial selection on disease-associated metabolites, every case group and wild-type comparisons were evaluated by Kruskal−Wallis (KW) analysis of variance (ANOVA) on ranks. This was performed using the software package MATLAB version 9 (The MathWorks, Inc., Natick, MA). Metabolites, whose Benjamini−Hochberg p-values < 0.05, were putatively annotated by comparison of their migration time and spectra with an in-house library of pure standards and the METLIN Metabolomics Database.[21]

GC-QTOF/MS Analysis

The above-described dried samples were resuspended in 450 μL of MeOH/H_2O/MTBE (74:10:16), and after centrifugation at 12 600*g*, 15 min at 4 °C, the supernatant was transferred to a vial with an insert and evaporated to dryness under high vacuum. The obtained dried extracts were derivatized by an MPS autosampler for GC/MS analysis as previously described by Fiehn.[22] Briefly, aldehyde and keto groups were first converted to *O*-methyloximes by reaction with 10 μL of pyridine containing 15 mg·mL^{-1} *O*-methoxyamine (Sigma-Aldrich, Germany) for 60 min at 70 °C. In a second step, acid hydrogen-containing metabolites were trimethylsilylated by reaction with 10 μL of *N*,*O*-bis(trimethylsilyl)-trifluoroacetamide (BSTFA) (Sigma-Aldrich, Germany) to enhance the GC/MS metabolite coverage.

The analysis was performed on an Agilent Technologies 7890B GC system equipped with a Gerstel MPS autosampler and an Agilent Technologies 7200 accurate mass Q/TOF analyzer equipped with an electron ionization (EI) source. Then, 1 μL of the sample was injected into a multimode inlet at 230 °C with the split ratio set at 1:12 with 9.354 mL·min^{-1} connected to a capillary column (30 m × 0.25 mm × 0.25 μm; Agilent, Germany). Helium was used as the carrier gas, at a flow rate of 0.78 mL·min^{-1}. Column temperature was 60 °C for 1 min and then programmed to increase at a rate of 10 °C·min^{-1} until 325 °C, which was maintained for 10 min. The total runtime was 37.5 min. The MS scan mode was chosen as the acquisition mode, with the mass range of 50−650 m/z and an acquisition rate of 10 spectra·s^{-1}.

The individual analytical fingerprints obtained were deconvoluted using MassHunter Unknown Analysis version B.07.00. This software also allows for the annotation of metabolites comparing the mass spectrum obtained with those of a target compound library, FiehnLib, and as this FiehnLib library includes retention indices, the retention time was also used as an additional criterion.[23]

After applying the MassHunter Unknowns Analysis, a.cef file including the compound name, mass, CAS number, formula, and retention times was generated to create a method for the MassHunter Quantitative Analysis version B.07.00 to export a data matrix containing integrated areas for each compound. Signals derived from the column bleed were eliminated; afterward, the abundances were normalized using the mean fold-change method of normalization.

LC-QTOF/MS Analysis

The above-described dried samples were resuspended in 200 μL of methanol/water/MTBE (7.4:1:1.6), vortexed for 1.5 h, and centrifuged (4000*g*, 10 min, 4 °C). Clear solutions were analyzed by LC-QTOF/MS. An HPLC system (1200 series, Agilent Technologies, Waldbronn, Germany), equipped with a degasser, two binary pumps, and a thermostated autosampler coupled to an Agilent 6520 QTOF/MS system (Agilent Technologies, Waldbronn, Germany), was used in both positive and negative ESI polarity modes to increase the metabolome coverage.

Briefly, 5 μL of extracted lung samples was injected into a thermostated (60 °C) Agilent Poroshell 120 EC-C8 column (150 mm × 2.1 mm, 2.7 μm; Agilent Technologies, CA) with a guard column Ascentis Express C8 (5 mm × 2.1 mm, 2.7 μm; Supelco, Bellefonte, PA). The flow rate was 0.4 mL·min^{-1} with solvent A (10 mM ammonium formate in Milli-Q water) and solvent B (10 mM ammonium formate in methanol and 15% isopropanol) for analysis in the positive ionization mode and solvent A (Milli-Q water with 0.1% formic acid) and solvent B (methanol with 0.1% formic acid and 15% isopropanol) for analysis in the negative ionization mode. Initial conditions at time 0 were 82% B, increasing to 96% B in 30 min. This was then held until 38 min. The gradient then increased to 100% B by 38.5 min and held until 40.5 min. The conditions were then returned to the starting conditions by 42 min, followed by an 8 min re-equilibration time. The total runtime of the method was 50 min. Capillary voltage was set to 4.5 kV; the drying gas flow rate was 10 L·min^{-1} at 350 °C and gas nebulizer at 40 psi; fragmentor voltage, skimmer voltage, and octopole radio frequency voltage were set to 175, 65, and 750 V, respectively. Data were collected at a scan rate of 1.05 spectra·s^{-1}. Mass spectrometry detection was performed in both positive and negative ESI modes in a full scan from 100 to 1000 m/z. Samples were analyzed in separate runs (positive and negative ionization modes), in a randomized order. The resulting LC-QTOF/MS data files were cleaned of background noise and unrelated ions by the Batch Recursive Feature Extraction tool with Agilent MassHunter Profinder software version B.06.00. Data were extracted using data-mining algorithms of the software. Putative annotation of metabolites found in positive and negative

https://dx.doi.org/10.1021/acs.jproteome.9b00868
J. Proteome Res. 2020, 19, 2053−2070

ionization modes was performed by the CEU Mass Mediator[24] for a subset of metabolites as described above for CE-TOF/MS. Univariate statistical significance was determined by the Kruskal–Wallis (KW) test as described above for CE-TOF/MS.

Van Krevelen Diagrams

Oxygen-to-carbon and hydrogen-to-carbon ratios were calculated for subsets of metabolites, whose putative annotations led to one possible chemical formula. The resulting data was plotted in a previously described metabolic map.[25]

Statistics

To productively mine large data sets from multiplatform HRMS-based metabolomic approaches, a robust and reproducible statistical data pipeline is necessary (Figure 1A).[26] To obtain a global view of results arising from different analytical platforms (Supporting Table S1), results were combined using the consensus orthogonal partial least squares-discriminant analysis (cOPLS-DA) data fusion algorithm.[27] OPLS-DA-related algorithms calculate mathematical projections, which explain the maximum variability between previously assigned sample groups for a specific metabolite data matrix. In this context, cOPLS-DA is a multivariate statistical test, which allows a joint interpretation of the results from multiple analytical platforms in a single analysis, performed on a merged multiplatform data set. Contrarily to the traditional OPLS-DA, which penalizes the importance of metabolite alterations from smaller metabolic data sets, cOPLS-DA harmonizes the data structure by performing a weighted normalization of each MS platform-specific data matrix, contextualizing and scoring the contribution of individual metabolites of the entire multiplatform data set to an optimally discriminant, group-specific metabolic fingerprint within the data model. Pairwise cOPLS-DA comparisons between uninfected mice and mice 4 and 9 weeks postinfection were generated. Additionally, a cOPLS-DA model including all sample groups was also calculated. Note that cOPLS-DA, as well as OPLS-DA, does not determine a specific cutoff value for determining statistical significance. Then, a quantitative value assessing the variable importance in the projection is assigned to each metabolite in the context of a metabolite data matrix. Therefore, although metabolites with variable importance in the projection (VIP) values > 1 not including 0 in the error confidence interval are generally accepted as statistically relevant, it cannot be assumed that metabolites with lower VIP values do not contribute to the multivariate separation and differences observed between the sample groups. Additionally, a shared and unique structure (SUS) plot was generated to evaluate the differential trends in metabolites across the disease time points.

Bioinformatics

As a first approach to highlight altered biological pathways, MetaboAnalyst (version 4.0)[28] was employed to map the metabolites with VIP values higher than 1, using metabolite enrichment analysis (overrepresentation analysis and pathway analysis). To reduce the possible bias induced by signals with more than one tentative annotation, a curated input subset of unique metabolites with their respective KEGG code identifiers (Supporting Table S1) was generated. However, given the inherent bias of enrichment algorithms since metabolomic analyses do not entirely cover the enrichment sets and pathways constitute a classical "dissection" of the metabolome, we also exploited clustering and metabolic network modularity analyses, which can be exploited to explore the influence of metabolites on each other based on their mathematical relationships and the network topology, respectively.

Overrepresentation Analysis. Representation of metabolites with VIP > 1 values determined in cOPLS-DA models, including all pairwise comparisons and a three-group comparison, was obtained by the performance of hypergeometric tests in pathway-associated metabolite sets, using the default reference metabolome. Significance of metabolite sets was assessed by a *p*-value cutoff of 0.05.

Pathway Analysis. Metabolite representation and pathway impact were assessed by the performance of hypergeometric tests and evaluation of the relative-betweenness centrality of the metabolites in the *Mus musculus* pathway library for each subset of metabolites with VIP > 1 values determined in all generated cOPLS-DA models. All of the compounds present in the selected pathways were considered. Significance of metabolite sets was assessed by a *p*-value cutoff of 0.05.

Metabolite Clustering Analysis and Heatmap Generation. The entire data matrix resulting from data processing and annotation, as well as specific subsets of metabolites, was loaded onto the MetaboAnalyst 4.0 server.[28] A hierarchical clustering of both samples and metabolites was performed using the whole matrix input and using MetaboAnalyst default parameters (Supporting Figure S1). The different heatmaps highlighted in the Results and Discussion section were generated in parameter consistency with the whole-data matrix heatmap, although no clustering was performed.

Metabolic Subnetwork Generation and Network Clustering Analysis. Metabolite-specific and generic compound KEGG codes[29] were assigned to all metabolites with unique annotations. A metabolic subnetwork based on KEGG RPAIR data was generated using MetaboNetworks (version 2.1)[30] and converted to .sif format (Supporting Text File S1). After deletion of duplicated edges, the subnetwork modularity was evaluated using the ModuLand (version 2.0)[31] Plug-in for Cytoscape (version 3.6.1).[32] ModuLand 2.0 employs a community landscape approach, which uses the LinkLand algorithm for calculating influence functions of each node in the whole node data set and the ProportionalHill method to determine the different discrete or overlapping modules present in the subnetwork, besides highlighting central node representatives of the different clusters and nodes bridging between clusters.[33] Once the modules are determined, ModuLand 2.0 merges them as metanodes and iteratively runs the algorithm, providing different hierarchical levels of the network. Both discrete and overlapping modularity algorithms were run. After merging of modules with correlation values higher than 0.9, the discrete modularity algorithm was used for careful data interpretation.

RESULTS AND DISCUSSION

cOPLS-DA of Multiplatform HRMS-Based Metabolomics Reveals Significant, Time-Dependent Changes in the Lung Metabolome of *Mtb*-Infected Mice

C57BL/6 mice were infected with *Mtb* H37Rv and euthanized at 4 and 9 weeks postinfection. Metabolome analyses were limited to the 4-week time point, which reflects induction of adaptive immunity, and the 9-week time point, which reflects established, chronic disease. Since multiplatform HRMS requires the processing and analysis of large numbers of samples, for purposes of practicality, only these two time points were chosen. Lungs were removed from uninfected (Mtb^-), 4 weeks

https://dx.doi.org/10.1021/acs.jproteome.9b00868
J. Proteome Res. 2020, 19, 2053−2070

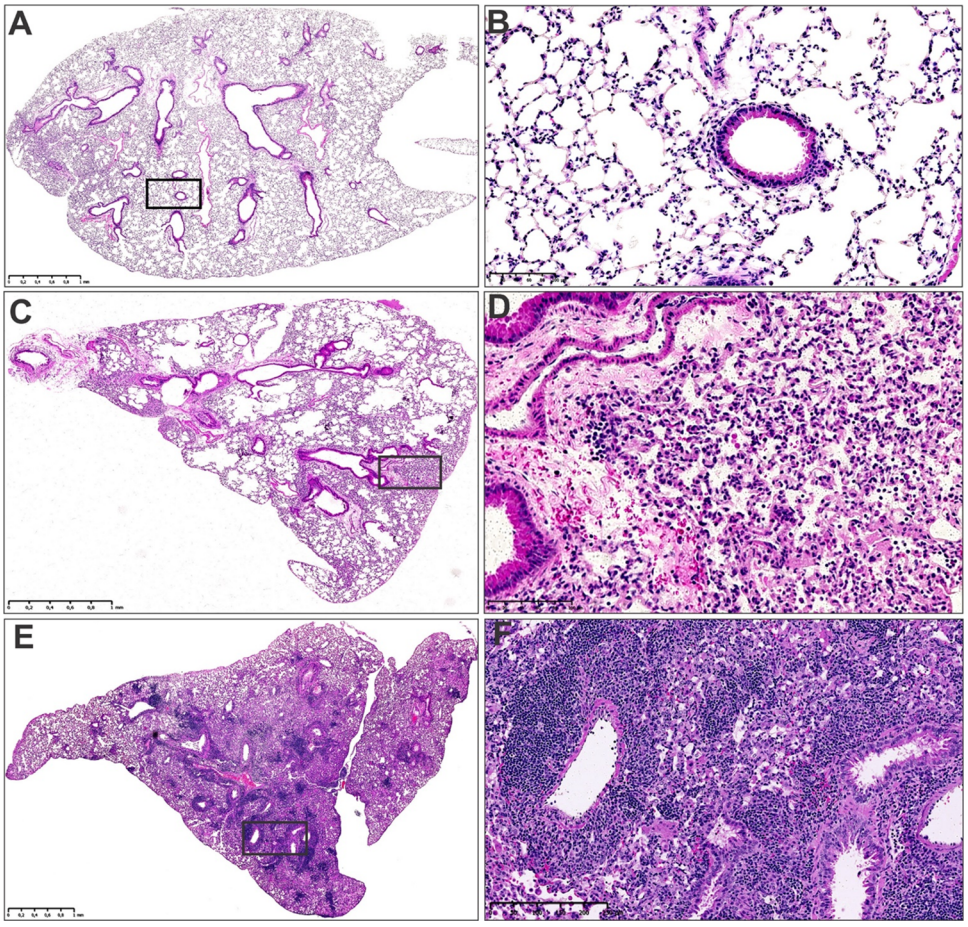

Figure 2. Representative images of the histomorphology of uninfected and *Mtb*-infected mouse lungs. Low-power (A) and high-power (B) Hematoxylin and Eosin staining (H&E) of uninfected control mouse lungs. Low-power (C) and high-power (D) H&E of *Mtb*-infected mouse lungs at 4 weeks postinfection. Low-power (E) and high-power (F) H&E of *Mtb*-infected mouse lungs at 8 weeks postinfection. Note the progressive increase in alveolar consolidation of the infected lung tissue (C, D, E, F), which is absent in the uninfected lung tissue (A, B).

(*Mtb*$^+$4*w*), and 9 weeks (*Mtb*$^+$9*w*) postinfection mice. Lesions were clearly visible in the lungs of infected mice, albeit more severe pathology was noted in *Mtb*$^+$9*w* compared to *Mtb*$^+$4*w* (Figure 2).

Metabolites were extracted from the lungs and analyzed separately by three HRMS-based platforms (LC-QTOF/MS, GC-QTOF/MS, and CE/TOF-MS). Overall, the different metabolomic platform analyses revealed a notable joined matrix data set of 1215 potential compounds after data processing and curation, where 456 metabolites were putatively annotated (Supporting Table S1). In the cOPLS-DA models, 554, 638, and 546 potential compounds from the entire metabolite data set scored VIP values > 1 for *Mtb*$^+$4*w*/*Mtb*, *Mtb*$^+$9*w*/*Mtb*$^-$, and *Mtb*$^+$9*w*/*Mtb*$^+$4*w* pairwise comparisons, respectively (Table 1). Additionally, a three-group comparison determined 631 potential compounds with VIP > 1 values. These results suggest that profound changes in the metabolome occur during *Mtb* infection.

Prominent group clustering and separation were observed in the cOPLS-DA score plots (Table 2 and Figure 3A). Given the high model fit (R^2Y) and prediction accuracy (Q^2Y) values found in cOPLS-DA models, the most striking results that emerged from the data are that strong, time-dependent quantitative metabolic abnormalities occur in the lung of all disease groups. Interestingly, each HRMS-based analysis contributed to explaining additional group separation between the different comparisons. In addition, distinct values were determined for the specific contribution of each HRMS-based metabolomic platform to the strength of the model components. These observations demonstrate the importance of multiplatform analyses in obtaining metabolomic data capable of achieving enhanced metabolome coverage and producing increased phenotype-associated group separation in multivariate analyses (Table 2).

Table 1. Detected, Annotated, and Statistically Significant Potential Compounds

		variable importance in the projection (VIP) > 1			
analytical platform	annotated/ total	*Mtb*$^+$9*w*/ *Mtb*$^+$4*w*/ *Mtb*$^-$	*Mtb*$^+$4*w*/ *Mtb*$^-$	*Mtb*$^+$9*w*/ *Mtb*$^-$	*Mtb*$^+$9*w*/ *Mtb*$^+$4*w*
GC-QTOF/MS	100/107	54	46	51	48
CE-TOF/MS	127/268	153	119	152	119
LC-QTOF/MS$^+$	182/643	319	294	337	280
LC-QTOF/MS$^-$	48/197	105	95	98	99
sum	457/1215	631	554	638	546

https://dx.doi.org/10.1021/acs.jproteome.9b00868
J. Proteome Res. 2020, 19, 2053−2070

Table 2. Model Fit, Prediction Accuracy, and Technique-Dependent Contribution Values to the Separation Observed in the Different cOPLS-DA Models[a]

model	R^2Y	Q^2Y	A	GC-QTOF/MS	CE-TOF/MS	LC-QTOF/MS$^+$	LC-QTOF/MS$^-$
Mtb$^+$9*w*/*Mtb*$^+$4*w*/*Mtb*$^-$	0.976	0.886	tp1	0.23	0.30	0.22	0.26
			tp2	0.25	0.19	0.27	0.29
			to	0.26	0.20	0.34	0.20
Mtb$^+$4*w*/*Mtb*$^-$	0.999	0.919	tp1	0.25	0.23	0.25	0.27
			to	0.27	0.27	0.26	0.20
Mtb$^+$9*w*/*Mtb*$^-$	0.994	0.936	tp1	0.22	0.28	0.24	0.26
			to	0.19	0.15	0.43	0.23
Mtb$^+$9*w*/*Mtb*$^+$4*w*	0.995	0.885	tp1	0.23	0.26	0.23	0.28
			to	0.23	0.23	0.30	0.24

[a]R^2Y, model fit; Q2Y, predictive accuracy; tp, predictive principal component; to, orthogonal principal component.

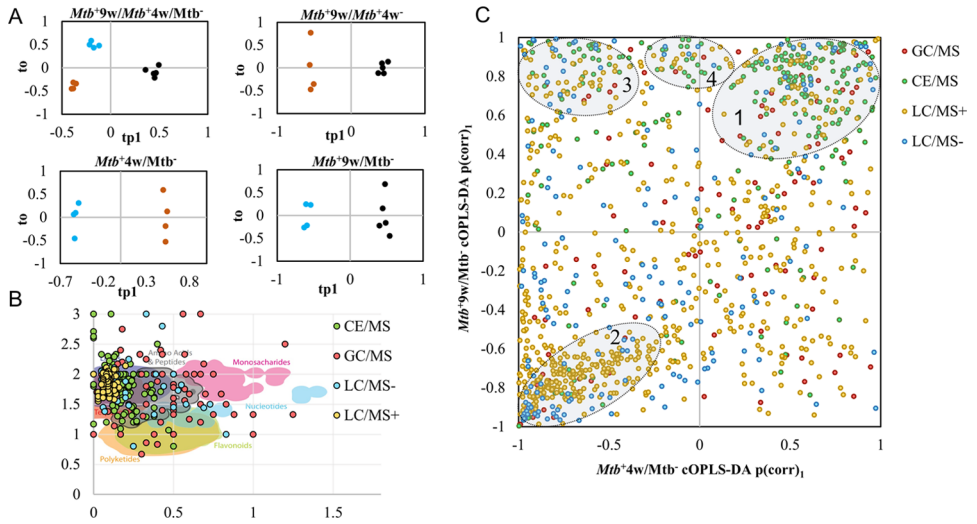

Figure 3. cOPLS-DA, Van Krevelen, and SUS plots describing the metabolite data set. (A) cOPLS-DA score plots of *Mtb*$^+$9*w*/*Mtb*$^+$4*w*/*Mtb*$^-$ and pairwise comparisons. (B) SUS plot of potential compounds for *Mtb*$^+$9*w*/*Mtb*$^-$ and *Mtb*$^+$4*w*/*Mtb*$^-$ comparisons. (C) Van Krevelen diagram of putatively annotated metabolites showing the metabolite distribution according to their molecular formula. In cOPLS-DA score plots, *Mtb*$^-$ represents blue, *Mtb*$^+$4*w* represents brown, and *Mtb*$^+$9*w* represents black. LC/MS$^+$ and LC/MS$^-$ represent positive and negative ESI polarity modes, respectively. In the SUS plot, clusters 1 and 2 represent direct shared structures of metabolites consistently increased and decreased at both time points, respectively. Cluster 3 represents a group of metabolites with an inverse shared structure, while cluster 4 encompasses metabolites increased only in *Mtb*$^+$9*w*.

Three major clusters of metabolites could be observed among statistically significant metabolites in the shared and unique structure (SUS) plot (Figure 3B). The first and second clusters of metabolites encompassed the majority of metabolic alterations and corresponding metabolites whose levels follow a similar trend at both disease stages. A third cluster represented metabolites that decreased at *Mtb*$^+$4*w* and increased at *Mtb*$^+$9*w*. A smaller, fourth cluster represented metabolites that were exclusively increased at *Mtb*$^+$9*w*, therefore representing a specific, late alteration during advanced TB. These results showed that although most of the alterations were consistently increased or decreased at both infection time points, the abundances of a considerable subset of metabolites were altered between the two infection time points. Therefore, a clear phenotypic difference could be detected between *Mtb*$^+$4*w* and *Mtb*$^+$9*w* mice. This emphasizes the importance of sampling metabolites at multiple time points during infection to describe the phenotypic characteristics of the progression of pulmonary TB. Clustering analysis of samples and potential compounds indicated that *Mtb*$^+$4*w* separates from *Mtb*$^+$9*w* and *Mtb*$^-$ samples (Supporting Figure S1). These results indicate that the metabolic phenotype of *Mtb*$^+$4w is notably altered, suggesting an early response to TB infection, which is partially reversed in *Mtb*$^+$9*w*. The different clusters of metabolites were in excellent agreement with the data obtained from the SUS plot.

The annotated metabolome was notably enriched in different metabolite classes including carbohydrates, small organic acids, amino acids, peptides, and lipidome-related compounds, thereby representing a broad overview of the metabolome (Figure 3C). In the context of TB, alterations in the levels of these metabolite pools should be carefully interpreted. For example, mass exchange occurs within several animal compartments and the environment, as well as cross-talking between different compartments (i.e., migration and proliferation of macrophages and T lymphocytes in the lung[34] and stratified macrophage polarization in *Mtb* granulomas[35,36]), to modulate the spatiotemporal distribution of metabolites. In addition, lysis and extraction of a tissue sample prior to analysis trigger a loss of compartmentalization and spatial information.[37] As a consequence, metabolite levels in the tissue are not only the result of a superimposition of the different metabolite concentrations in all of the tissue and cellular compartments from both *Mtb* and mouse metabolomes but also the result of the interaction of both genomes, the so-called cometabolome (i.e., *Mtb*-secreted proteins that metabolize macrophage metabolites).[38] Next, we

https://dx.doi.org/10.1021/acs.jproteome.9b00868
J. Proteome Res. 2020, 19, 2053−2070

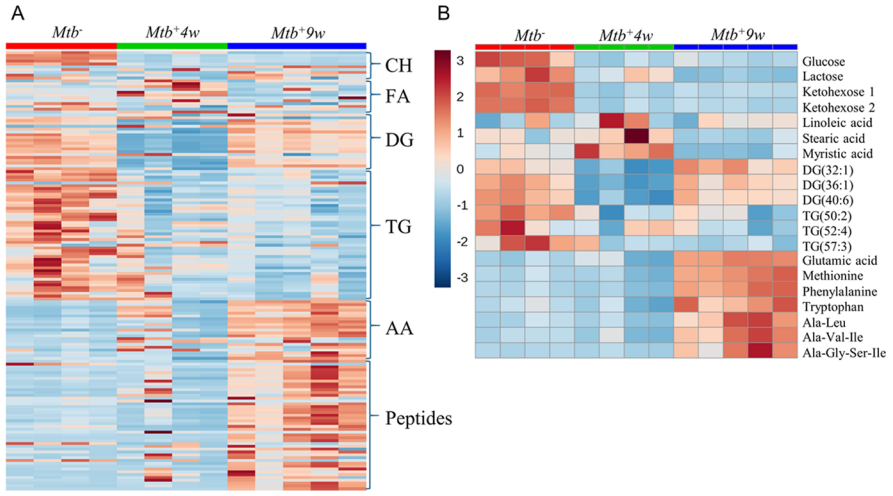

Figure 4. Heatmaps depicting the metabolic changes associated with major nutrient groups during disease progression. (A) Overall metabolic-associated changes. Note the prominent changes in carbohydrates and energy-storage-related lipids, whereas increasing abundances of amino acids and oligopeptides occur with disease progression. (B) Representative selected metabolic changes. CH, carbohydrates; FA, fatty acids; DG, diacylglycerols; TG, triacylglycerols; AA, proteinogenic amino acids annotated in the study at 0 (Mtb^{-}), 4 ($Mtb^{+}4w$), and 9 ($Mtb^{+}9w$) weeks postinfection.

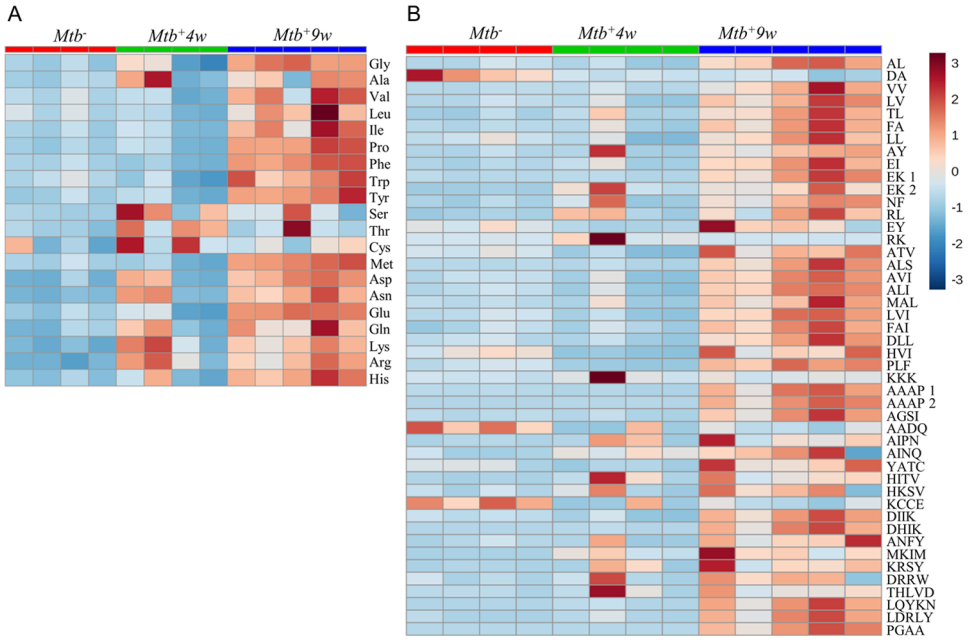

Figure 5. Detailed heatmap representations depicting *Mtb*-associated amino acid and peptide abundance changes during disease progression. (A) Proteinogenic amino acid abundances. (B) Oligopeptide abundances annotated in the study. Note that oligopeptide annotations are indicative, since CE-TOF/MS cannot determine the amino acid sequence. A gradual increase in the levels of the majority of metabolites grouped in this section occurs with the disease progression.

investigated changes in these metabolite classes in more detail in the context of disease progression.

Systematic Overrepresentation (ORA) and Pathway Analysis (PA) Identified Disease-Specific Pathways Altered in *Mtb*-Infected Mice

To obtain functional information from differentially regulated metabolic pathways, two enrichment analyses were performed. First, we performed an overrepresentation analysis (ORA), in which significantly different metabolic alterations were identified (Supporting Table S3). These mainly encompassed the metabolism of amino acids and phospholipids. Overall, the ORA results point toward an alteration of phospholipid metabolism in $Mtb^{+}4w$, which unexpectedly returned to nonsignificant values at $Mtb^{+}9w$. To further support the data obtained by ORA, pathway analysis was performed as a second enrichment algorithm. In this context, PA mostly detected metabolite sets consistently altered in ORA (Supporting Table S3), including the metabolism of phospholipids, amino acids, and nitrogen. Additional alterations in metabolic pathways not identified by ORA were reported as significant in $Mtb^{+}4w/Mtb^{-}$ (propanoate metabolism) and $Mtb^{+}9w/Mtb^{-}$ (β-alanine metabolism) or both (sphingolipid, glutathione metabolism), demonstrating the need for different algorithms to provide a more holistic data analysis to identify relevant biological processes during the progression of pulmonary TB.

https://dx.doi.org/10.1021/acs.jproteome.9b00868
J. Proteome Res. 2020, 19, 2053−2070

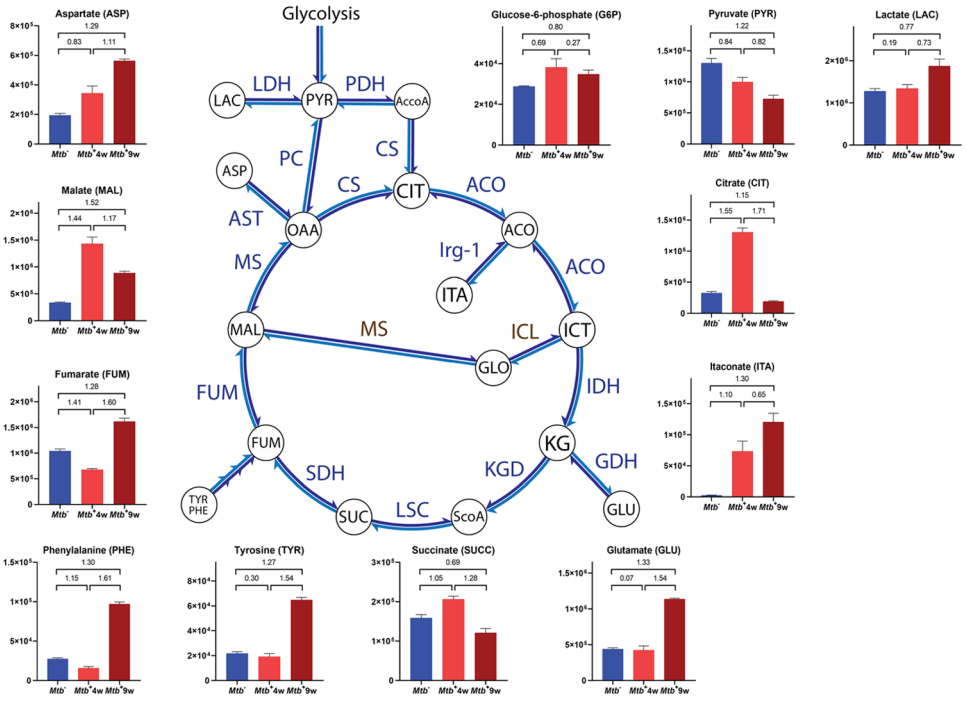

Figure 6. Topology of the TCA and related pathways and *Mtb*-associated semiquantitative changes. Graphs represent arbitrary normalized abundance units and VIP values between pairwise comparisons. *Y*-axes on graphs represent arbitrary normalized abundance units. VIP values between pairwise comparisons are indicated. Metabolites not appearing on graphs are abbreviated as follows: AccoA, acetyl-coenzyme A; ACO, aconitate; ICT, isocitrate; GLO, glyoxylate; KG, α-ketoglutarate; ScoA, succinyl coenzyme A; OAA, oxaloacetate; enzymes are colored in blue except for *Mtb*-specific enzymes, which are colored in brown; CS, citrate synthase; LDH, lactate dehydrogenase; PDH, pyruvate dehydrogenase; PC, pyruvate carboxylase; ACO, aconitase; Irg-1, immune-responsive gene 1 protein; ICL, isocitrate lyase; MS, malate synthase; IDH, isocitrate dehydrogenase; GDH, glutamate dehydrogenase; KGD, α-ketoglutarate dehydrogenase; LSC, succinyl-coA ligase; SDH, succinate dehydrogenase; FUM, fumarase; MS, malate synthase; AST, aspartate aminotransferase.

Macronutrient Consumption is Consistent with *Mtb*-Associated Wasting

Interestingly, three distinct responses in metabolite levels indicate macronutrient consumption (Figure 4A,B). In the first response, distinct carbohydrates showed a notable decrease in $Mtb^{+}4w$, which was maintained in $Mtb^{+}9w$. In the second response, triacylglycerols decreased in $Mtb^{+}4w$ and $Mtb^{+}9w$, and diacylglycerol metabolites showed an initial decline at $Mtb^{+}4w$ followed by a noticeable increase in $Mtb^{+}9w$, whereas the levels of several fatty acids increased in $Mtb^{+}4w$ and decreased at $Mtb^{+}9w$. The third response was represented by amino acids and oligopeptides, which progressively increase throughout the course of infection. Interestingly, the abundance of methylhistidine, which has been proposed as a biomarker of skeletal muscle breakdown and injury,[39,40] was notably increased in $Mtb^{+}9w$ (Supporting Table S4). Hence, high levels of methylhistidine suggest that muscle wasting occurs during advanced TB disease and are consistent with previous studies documenting a link between *Mtb* infection and malnutrition/wasting.[41,42] Overall, we posit that these data correspond with the induction of a temporal and progressive catabolic state in *Mtb*-infected mice, which is elicited to satisfy the continuously changing energy demand to control infection.

TB Disease Progression Correlates with an Increase in Proteolysis-Related Metabolites

Destruction of the extracellular matrix/pulmonary parenchyma is a well-documented phenomenon that occurs during *Mtb* infection.[43,44] Upon *Mtb*-induced macrophage activation, protein degradation is primarily performed through the activity of secreted matrix metalloproteinases (MMPs, mainly MMP-1 and MMP-9[43]). Surprisingly, a consistent increase in specific and nonspecific protein breakdown products was observed in *Mtb*-infected mice (Figure 5A,B and Supporting Table S4). Nonspecific metabolites included short oligopeptides, amino acids, and *N*-glycolylneuraminate. Specific protein degradation-associated metabolites included *trans*-4-hydroxyproline and galactosylhydroxylysine. These metabolites are related to collagen-like post-translational modifications, suggesting that substantial alterations occur in collagen and surfactant proteins SP-A and SP-D (which are essential components of the lung[45,46]) during disease. Lastly, increased abundances of a metabolite annotated as desmosine, a breakdown product of elastin, allude to increased elastin degradation in the TB lung. Elastin is a major component of the extracellular matrix of the lung. Upon lung injury, which involves the catabolism of the extracellular matrix and elastin, desmosine is released. Not surprisingly, desmosine has been identified as a potential biomarker for structural lung injury in pulmonary TB and chronic obstructive pulmonary disease.[47,48] Overall, we propose that the metabolites here constitute a data subset indicative of alveolar destruction (Figure 2), progressive proteolysis, and establishment of lung fibrosis[49,50] occurring during TB progression.

Increased Itaconic Acid (ITA) Production Subsequent to Alterations in the Central Carbon Metabolism Occurs in the Lungs of *Mtb*-Infected Mice

It is widely accepted that the central carbon metabolism constitutes a relevant link between energy production and immunity. In the context of carbohydrate metabolism, we

https://dx.doi.org/10.1021/acs.jproteome.9b00868
J. Proteome Res. 2020, 19, 2053−2070

detected carbohydrate depletion occurring upon *Mtb* infection (Figure 4) and moderate increases in glucose-6-phosphate (Figure 6), which suggested increased substrate availability for the pentose phosphate pathway (PPP), a major biosynthetic pathway for nucleotides and NADPH, which is required as a cofactor for glutathione reductase during oxidative stress and for inducible nitric oxide synthase (iNOS).[51] Intriguingly, lactate increased marginally in *Mtb*$^+$4*w* and moderately in *Mtb*$^+$9*w* (Figure 6), suggesting that most of the pyruvate was being utilized elsewhere at 4 weeks but converted into lactate at 9 weeks postinfection. In contrast, pyruvate progressively decreased with TB disease progression (Figure 6). Previous transcriptomics and immunofluorescence studies of *Mtb*-infected mouse lungs demonstrated increased expression of glycolytic enzymes, lactate dehydrogenase, and glucose transporters at 4 weeks postinfection, and it was concluded that the Warburg effect is induced in *Mtb*-infected mouse lungs.[52] However, the marginal increase we observed in lactate in *Mtb*$^+$4*w* does not fully support these findings and also differs from a previous NMR mouse study,[16] where lactate levels were examined at a single, early time point (28 days postinfection). In the guinea pig model for TB, NMR studies have shown a decrease in serum lactate levels but an increase in lung lactate levels.[18] Overall, these findings point to the spatiotemporal regulation of lactate, which differs in different animal model systems. The large increase in citrate in *Mtb*$^+$4*w* (Figure 6) suggests that most of the pyruvate is being converted into citrate in *Mtb*$^+$4*w* for fatty acid synthesis and initial production of itaconate during the early induction of adaptive immunity.[53,54] However, the substantial decrease in citrate at 9 weeks postinfection is likely due to the formation of the remarkably high levels of ITA present in *Mtb*$^+$9*w* (Figure 6). This observation is consistent with previous NMR studies reporting increased itaconate levels during *Mtb* infection.[16]

Itaconate is biosynthesized from *cis*-aconitic acid by decarboxylation performed by the immune-responsive gene 1 protein (IRG-1), whose gene (*Irg*1[55]) is upregulated in macrophages upon stimulation with LPS, TNF-α, and IFN-γ.[56,57] Not surprisingly, itaconate plays several roles in immunometabolism. ITA has been shown to play a major role in metabolic reprogramming through inhibition of the TCA enzyme succinate dehydrogenase (SDH)[58] and to exert direct antibacterial activity through inhibition of bacterial isocitrate lyase.[59,60] Given the relevance of itaconate in TB,[61] we speculate that at 4 weeks postinfection, pyruvate is being redirected to increase citrate levels necessary for fatty acid synthesis and ITA production. However, when chronic infection sets in at 9 weeks, we surmise that the citrate levels are substantially reduced to generate higher levels of ITA necessary to subdue the inflammatory response.

The TCA cycle in inflammatory macrophages has breakpoints at SDH and isocitrate dehydrogenase.[54,62] In addition, it has been described that ATP generation in effector T-cells relies on glycolysis, rather than OXPHOS.[63] Alterations in several TCA-related metabolites (Figure 6 and Supporting Table S4) propose similar observations at *Mtb*$^+$4*w*, including (i) increased citrate accumulation in *Mtb*$^+$4*w*; (ii) possible SDH inhibition supported by increased succinate and itaconate abundances in *Mtb*$^+$4*w*; (iii) possible malate dehydrogenase (MDH) inhibition, supported by reduced fumarate levels and increased malate and citrate in *Mtb*$^+$4w (which act as MDH inhibitors);[64] and (iv) NAD$^+$ modulation (Supporting Table S2). During the early stages of infection (*Mtb*$^+$4*w*), notable alterations in the levels of NAD$^+$ occur in the lung of infected mice, which has been also reported to occur in C57BL/6 mice using NMR.[16] More interestingly, the levels of nicotinamide, determined as the breakdown product of two *Mtb* NAD$^+$ glycohydrolases (MbcT and TNT,[65,66] the latter identified as relevant in *Mtb* pathogenesis),[67] were notably increased in *Mtb*$^+$4*w* (Supporting Table S4). However, these changes in NAD$^+$ and nicotinamide could also be a consequence of the host-related metabolic activity.[68] At *Mtb*$^+$9*w*, succinate levels and malate levels were decreased with a contrasting increase in fumarate levels. The high glutamate levels are possibly due to the accumulation of succinate from the inhibition of succinate dehydrogenase and the proteolysis discussed above (Figure 5A,B and Supporting Table S4). The high aspartate level, which is a proxy for oxaloacetate, is probably due to transamination reactions with high levels of glutamate.

Taken together, these results suggest that the observed TCA metabolic alterations are the outcome of a complex host-pathogen regulatory network (Figure 6) wherein the lung in *Mtb*$^+$4*w* resembles an inflammatory immunometabolic response, which are not fully maintained in *Mtb*$^+$9*w* as citrate levels are significantly decreased. In this context, it is important to point out that itaconate production is a marker for anti-inflammatory cellular responses induced following proinflammatory stimulation.[69] Thus, the metabolic alterations observed in the TCA cycle between the two time points suggest transitions between inflammatory and anti-inflammatory responses described in several studies.[63,65] Given the notable alterations in NAD-related metabolites occurring in *Mtb*$^+$4*w*, we suggest that the potential modulatory role of *Mtb* in NAD$^+$ metabolism occurring in the TB lung should be addressed further in future studies.

Mtb Disease Causes Alterations in Oxido-Reductive Stress-Related Metabolites

Mtb-induced inflammatory activation leads to the generation of reactive oxygen and reactive nitrogen species (ROS and RNS, respectively).[70] Consistently, the increase in arginine and citrulline levels in *Mtb*$^+$4*w* and *Mtb*$^+$9*w* is likely a consequence of the increased expression of inducible nitric oxide synthase (iNOS) in the lung (Supporting Table S4).[71] However, the presence of increased nitric oxide in infected cells is controversial, since it is also known that *Mtb* induces the expression of host arginase in infected macrophages.[72] Additionally, altered levels of xanthine and hypoxanthine (Supporting Table S4) point to substantial modulation in xanthine oxidase (XO) activity, which constitutes a major regulator of the superoxide ion ($O_2^{\bullet-}$). Interestingly, the abundances of xanthine and hypoxanthine levels were decreased in *Mtb*$^+$4*w*, whereas they were notably increased in *Mtb*$^+$9*w*, suggesting a differential behavior of XO with disease progression. During *Mtb* infection, NADPH oxidase (NADPHox) is another key enzyme that produces $O_2^{\bullet-}$ during the oxidative burst.[73] Although metabolites involved in NADPH production could not be detected, it is reasonable to infer that enhanced glucose-6-phosphate levels generate more substrates for NADPH production through the PPP.[74] However, it has been reported that MbcT hydrolyzes NAD$^+$,[67] and TNT is able to degrade both NAD$^+$ and NADP$^+$,[66] as mentioned above. Given that NADPHox and XO/iNOS require NADPH and NAD$^+$ as cofactors, respectively, we suggest that *Mtb*-mediated NAD(P)$^+$ glycohydrolase activity in modulating ROS/RNS production should be assessed in further studies. Overall, we identified a

https://dx.doi.org/10.1021/acs.jproteome.9b00868
J. Proteome Res. 2020, 19, 2053−2070

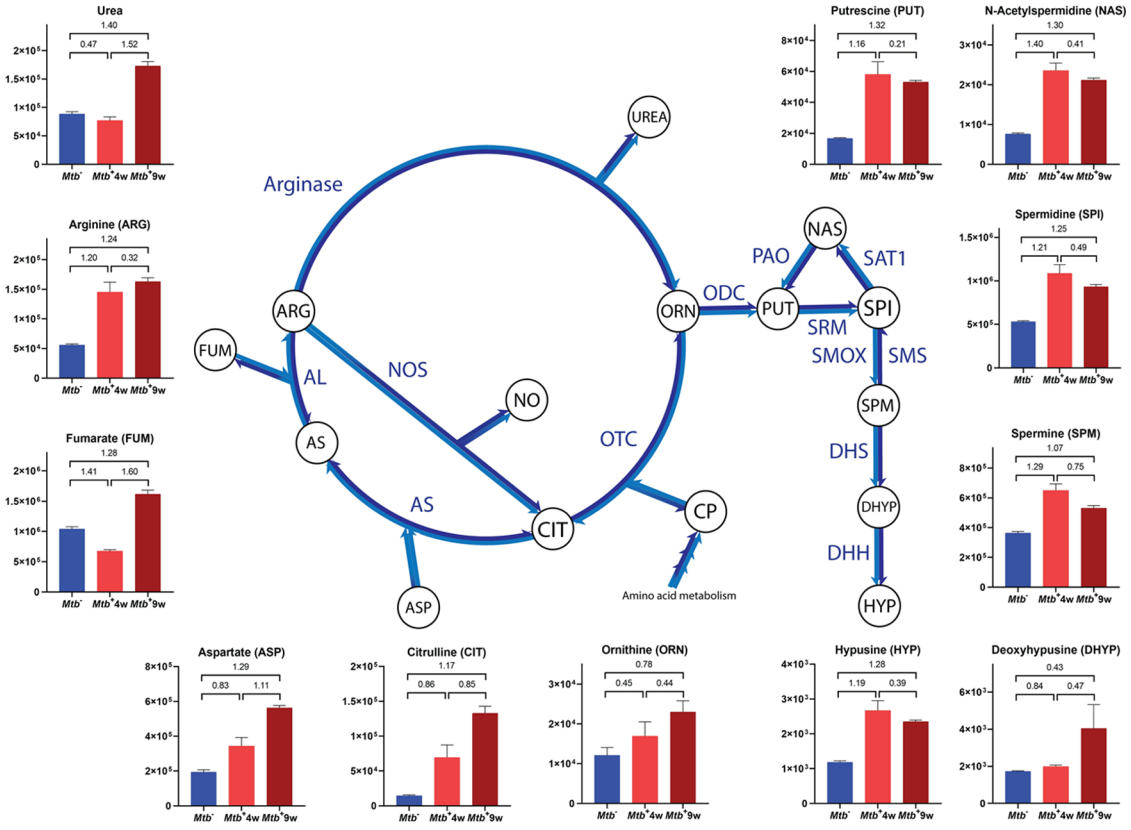

Figure 7. Topology of the urea cycle and polyamine biosynthesis pathways and *Mtb*-associated semiquantitative changes. *Y*-axes on graphs represent arbitrary normalized abundance units. VIP values between pairwise comparisons are indicated. Metabolites not appearing on graphs are abbreviated as follows: CP, carbamoyl phosphate; NO, nitric oxide; AS, argininosuccinate. Enzyme abbreviations are colored in blue: OTC, ornithine transcarbamoylase; AS, argininosuccinate synthase; AL, argininosuccinate lyase; NOS, nitric oxide synthase; ODC, ornithine decarboxylase; SRM, spermidine synthase; SMS, spermine synthase; SMOX, spermine oxidase; SAT1, spermidine/spermine-N^1-acetyltransferase; PAO, polyamine oxidase; DHS, deoxyhypusine synthase; DHH, deoxyhypusine hydrolase.

distinct subset of metabolites involved in ROS/RNS biosynthetic pathways, which provides compelling evidence that *Mtb* triggers time-dependent alterations in oxidative stress-related metabolites during infection.

Glutathione- and glutathione-related compounds play a key role in maintaining redox cellular homeostasis. Here, altered levels of reduced glutathione (GSH) and glutathione-derived products (oxidized glutathione (GSSG), *S*-lactoylglutathione, *S*-hydroxymethylglutathione) as well as glutathione precursors in *Mtb*$^+$4*w* and *Mtb*$^+$9*w* were detected (Supporting Table S4 and Figure 5A). Altered levels of these metabolites suggest modifications of the redox environment in the *Mtb*-infected lung. These results intimate an increase in de novo GSH synthesis, which could be an ROS-protective mechanism of the host while providing GSH-mediated direct antimycobacterial activity.[75,76] Generally, GSSG abundances were similar in *Mtb*$^+$4*w* and *Mtb*$^+$9*w*. The GSH/GSSG ratio returned to *Mtb*$^-$ levels in *Mtb*$^+$9*w*, suggesting the depletion of reduced glutathione with disease progression. This is supported by the alterations in metabolites related to the generation of ROS/RNS and the increase in glutathione-derived compounds observed in *Mtb*$^+$9*w*. Intriguingly, the abundances of *S*-lactoylglutathione were notably increased in *Mtb*$^+$4*w* and to a lesser degree in *Mtb*$^+$9*w*. This compound is primarily biosynthesized in the glyoxalase system, a metabolic pathway that is able to detoxify the cells from methylglyoxal, a glycolysis-derived compound. *S*-Lactoylglutathione is related to a plethora of immunity-related functions including phagocyte activation, anti-IgE-induced secretion of histamine in basophils, microtubule assembly, neutrophil granule secretion, and chemotaxis.[77] Thus, the levels found in our results suggest that dysregulation occurs in the glyoxalase system upon *Mtb* infection. Glyoxalase inhibition causes an accumulation of methylglyoxal, which has been described as cytotoxic for certain microorganisms such as *Staphylococcus aureus*[78] and *Plasmodium falciparum*.[77] Given this ex vivo observation, the pharmacological inhibition of the glyoxalase system-associated enzymes (GLO-I and GLO-II) may have modulatory activity in TB, as was previously proposed.[78]

Ergothioneine (EGT) is an antioxidant taken up from the environment by mammalian cells. However, *Mtb* also produces EGT, and it has been shown to be essential for survival in macrophages[79] and in mice.[80] Importantly, we found increased EGT levels at the late stage of infection (*Mtb*$^+$9*w*) (Supporting Table S4), which highlights the therapeutic potential of this antioxidant pathway.

Mtb Infection Drives Alterations in the Urea Cycle and Polyamine Metabolism

Important alterations in the urea cycle were found in both *Mtb*$^+$4*w* and *Mtb*$^+$9*w* (Figure 7 and Supporting Table S4). As explained above, augmented concentrations of arginine and citrulline may be regulated by altered iNOS activity, which generates citrulline and NO from arginine, thereby "bypassing" the urea cycle. However, the progressive increase in the expression of arginase mentioned previously[72] would favor the

https://dx.doi.org/10.1021/acs.jproteome.9b00868
J. Proteome Res. 2020, 19, 2053−2070

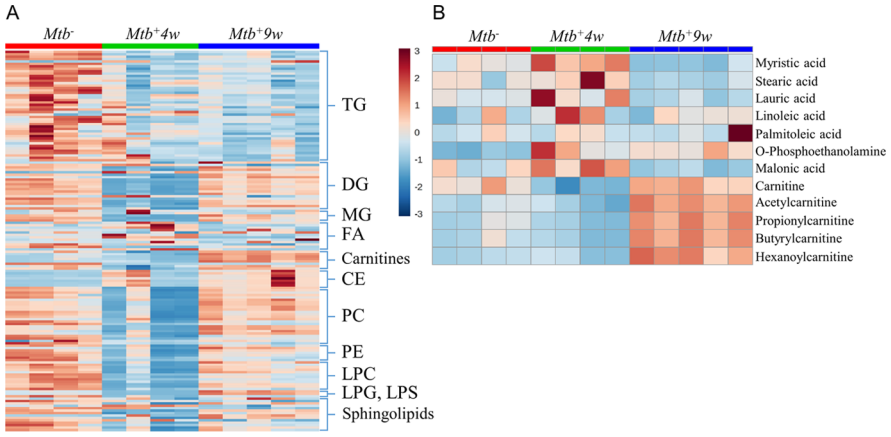

Figure 8. Heatmap representations of *Mtb*-associated lipidomic changes during disease progression. (A) Overall changes in different lipids, phospholipids, and carnitines. (B) Detailed changes in the abundances of selected fatty acids, carnitines, *O*-phosphorylethanolamine, and malonate. TG, triacylglycerols; DG, diacylglycerols; MG, monoacylglycerols; FA, fatty acids; CE, cholesteryl esters; PC, phosphatidylcholines; PE, phosphatidylethanolamines; LPC, lysophosphatidylcholines; LPG, lysophosphatidylglycerols; LPS, lysophosphatidylserines. Note that for most PC, LPC, DG, MG, and sphingolipids, the alterations in metabolite levels in *Mtb*$^+$4w are notably reversed in *Mtb*$^+$9w.

catabolism of arginine by arginase, thereby reducing RNS generation.[81] Therefore, increases in the levels of urea and ornithine observed in *Mtb*$^+$9*w* suggest a progressive anti-inflammatory metabolism. Alternatively, *Mtb*-associated wasting and the subsequent enhancement of protein catabolism for energy generation might explain a substantial part of the alterations in the urea cycle.

Consistent with these findings, increased levels of polyamines (i.e., spermidine, spermine, and putrescine) were found in both *Mtb*$^+$4*w* and *Mtb*$^+$9*w* (Figure 7 and Supporting Table S4). Polyamines are positively charged alkyl amines that interact with DNA and are essential for cell proliferation and adequate macrophage function,[82,83] although an immunosuppressive role has also been suggested.[84] Polyamines are also capable of binding iron, and interestingly, a link between ferritin H and polyamines during *Mtb* infection was recently established.[11] Endogenous polyamines have also been described as beneficial for *Mtb*, increasing the activity of *Mtb* RNA polymerase[85] and conferring fluoroquinolone resistance to the bacteria.[86] The increase in polyamine levels suggests that anti-inflammatory responses are present at both disease time points. Anti-inflammatory responses are associated with arginine catabolism through arginase activity, reducing NO production by iNOS.[11] Further studies on the modulation of enzymes involved in these pathways are expected to provide new insights into the polyamine-related immunometabolism of TB.

Polyamines also play an important role in protein translation since spermidine is a precursor for the synthesis of hypusine, which is increased in *Mtb*$^+$4*w* and *Mtb*$^+$9*w*. Hypusine is an amino acid exclusively found in the eukaryotic translation initiation factor 5A-1 (eIF-5A), which plays an important role in protein translation, particularly in the elongation step. Cell proliferation, ROS tolerance, mitochondrial function, and endoplasmic reticulum stress are a few examples of the variety of biological processes in which eIF-5A is involved.[87−89] Thus, increased levels of polyamines leading to increased levels of hypusine suggest altered activity of eIF-5A in *Mtb*-infected mice.

Mtb Infection Regulates Lipid Metabolism to Modulate Signaling and Immunity

We observed substantial variation in the lipidome over the course of infection (Figure 8A). *Mtb*$^+$4*w* mice show an overall decrease in the levels of triglycerides (TGs), diglycerides (DGs), monoglycerides (MGs), phosphatidylcholines (PCs), phosphatidylethanolamines (PEs), and lysophosphatidylcholines (LPCs), together with an increase in the levels of several free fatty acids (i.e., myristic, stearic, lauric, linoleic, palmitoleic) and *O*-phosphoethanolamine (Figure 8A,B and Supporting Table S4). These results suggest an increase in phospholipase and different lipase activities, which may contribute to the degradation of the main pulmonary surfactant lipid constituents.[90] These observations are of particular significance, as it could be argued that some of these lipids function as an in vivo carbon source for *Mtb*.[91] Hence, the depletion of triacylglycerols could be due to its hydrolysis by *Mtb*.[92] Our findings are consistent with previous studies demonstrating an increase in phospholipase A_2 (PLA_2) activity upon *Mtb* infection.[93] Furthermore, an increase in the abundance of malonic acid, a compound proposed as an indirect biomarker of fatty acid synthesis,[94] was detected in *Mtb*$^+$4*w* but decreased in *Mtb*$^+$9*w* (Figure 8B). Enhanced fatty acid synthesis in *Mtb*$^+$4*w* mice is also supported by the reduced levels of L-carnitine and acylcarnitines found in *Mtb*$^+$4*w* mice (Figure 8A,B). This correlates with the increase in the fatty acid synthase (FASN) activity that has been described in inflammatory macrophages and is regulated by the sterol regulatory element-binding transcription factor (SREBP1c).[95] Both PLA_2 and FASN activities have been demonstrated to exert proinflammatory effects.[93−96] Furthermore, fatty acid anabolism constitutes alternative pathways for NADPH generation and subsequent ROS formation, which is upregulated in inflammatory macrophages.[97,98] However, except for most TGs, the changes in the above-mentioned metabolites reflecting fatty acid synthesis are considerably reversed in *Mtb*$^+$9*w*, suggesting a possible attenuation of PLA_2 activity. Considering the carbohydrate depletion occurring in *Mtb*$^+$4*w* (Figure 4A,B), it is likely that *Mtb* causes a shift in metabolism toward fatty acid oxidation during disease. This is further supported by highly increased levels of carnitines (Figure 8A,B) found in *Mtb*$^+$9*w*. Such metabolic shifts correlate with the described capacity of *Mtb* to shift the macrophage from an inflammatory to an anti-inflammatory-like phenotype.[98,99]

Another interesting feature of *Mtb*-infected macrophages is the generation of cytosolic lipid droplets, which has been

https://dx.doi.org/10.1021/acs.jproteome.9b00868
J. Proteome Res. 2020, 19, 2053−2070

recently proposed to be a defense mechanism against infection, sequestering lipids to prevent carbon fueling of *Mtb*.[100] The composition of certain lipid droplets is rich in cholesteryl esters,[101] which have been found to be notably increased with disease progression. The notable increase found in cholesteryl esters suggests that foam cells accumulating cholesteryl esters in lipid droplets progressively increase in our disease model.[102,103] Consequently, it is highly likely that the Acyl-CoA cholesterol acyl transferase activity (ACAT) is increased in the lung of *Mtb*-infected mice.[11]

Sphingolipids, which are related to different immunomodulatory properties,[104] follow different patterns of expression in the diseased mice (Figure 8A). Regarding sphingolipid alterations occurring during TB disease, a decrease in the activity of sphingosine kinase (SphK) has been documented to occur in the lung of *Mtb*-infected mice, thereby blocking the Ca^{2+} influx toward the macrophage cytoplasm and thereby inhibiting the maturation of the phagosome.[105] Given the alterations found in our model and the reported evidence of sphingolipid metabolism modulation as a therapeutic strategy,[106] more lipidomic studies are needed to assess the importance of sphingolipids in *Mtb*-induced immune response.

Mtb Infection Dysregulates Purine and Pyrimidine-Related Metabolism

Overall, the levels of pyrimidine-related compounds increased, while purine-related compounds showed a complex profile (Supporting Table S4). Purine and pyrimidine-derived compounds participate in different biological processes including (i) DNA replication and RNA synthesis, and their demand is increased when cellular proliferation occurs; (ii) enzyme cofactors in reactions that require chemical energy (especially ATP) or a methyl donor (especially *S*-adenosylmethionine (SAM)); and (iii) signaling molecules through purinergic receptors. Our results suggest that these processes are strongly altered during *Mtb* infection. Interestingly, adenosine levels were decreased upon infection in both $Mtb^{+}4w$ and $Mtb^{+}9w$. Adenosine binds with high affinity to A_1, A_{2B}, and A_3 receptors, which are expressed by different cellular types of the immune system.[107] Activation of such receptors induces a variety of cellular functions, including secretion of pro- and anti-inflammatory cytokines, IgE production, mucous production, suppression of TNFα release, and bronchoconstriction.[107] Increased levels of adenosine might be the consequence of an increase in adenosine deaminase activity (ADA), which has been reported to occur in the bronchoalveolar lavage and serum of TB-infected patients.[108] In our model, depletion of adenosine implies diminishing ADO-mediated signaling through purinergic receptors while generating substrates for XO activity and subsequent ROS generation. AMP levels were increased in $Mtb^{+}4w$ and notably decreased in $Mtb^{+}9w$. Therefore, AMP could also be implicated in differential signaling through purinergic receptors with disease progression.[109]

Mtb Infection Dysregulates Smooth Muscle Physiology

In addition to the bronchodilator effect of NO release subsequent to increased iNOS activity,[110,111] significant alterations in metabolites that modulate lung smooth muscle tone were found (Supporting Table S4). With respect to bronchoconstrictors, the levels of acetylcholine, the main lung physiological bronchoconstrictor, were reduced in $Mtb^{+}4w$ and increased in $Mtb^{+}9w$, while histamine showed the opposite trend. Interestingly, serotonin and adenosine, which trigger bronchoconstriction in mice,[107,112] were decreased at both infection time points. Altogether, these results suggest an interplay between metabolite bronchoconstrictor and bronchodilator signals in which complex regulatory mechanisms are involved.

Trimethylamine-*N*-oxide (TMAO) Establishes a Metabolic Link between *Mtb* Infection and Cardiovascular Risk

The metabolic-associated changes mentioned in the above sections consider *Mtb* and the host as the sole metabolomes present in our study. However, this simplistic assumption does not consider the different bacterial communities that are continuously present in mice, including the gut and lung microbiomes.[113,114] This potentially expands the repertoire of bacterial-specific biosynthetic pathways during TB. For example, we detected high levels of TMAO in the lungs of *Mtb*-infected mice, especially in $Mtb^{+}4w$. Increases in TMAO were consistent with alterations in topologically related metabolites (Supporting Table S4). TMAO is a host flavin monooxygenase 3 (FMO3) degradation product of trimethylamine, a bacterial metabolite, which can be biosynthesized from different substrates, including choline, betaine, carnitine, and EGT.[115] Interestingly, RNA-seq experiments have pointed FMO3 to be related to the regulation of iron homeostasis during TB.[11] Although TMAO has been classically associated with the gut microbiome,[116] our data suggest that *Mtb* could be the biosynthetic source of trimethylamine. Hence, it seems reasonable that TMAO may serve as an electron acceptor for alternative *Mtb* respiration under anaerobic conditions, which was previously described for other bacteria (i.e., *Salmonella* spp., *Alteromonas* spp., *Vibrio* spp.[117]). Furthermore, increased TMAO levels have also been associated with induction of adhesion molecules and inflammation via NF-kB activation,[118] increased expression of murine macrophage scavenger receptors A and CD36, and inhibition of reverse cholesterol transport.[119] Lastly, our results suggest that TMAO is linked to lipid droplet and foam cell development during *Mtb* granuloma formation, which is consistent with recent studies assessing the role of TMAO in cardiovascular disease[120] and in line with the increased levels of cholesteryl esters as described above (Figure 8A). Overall, our findings identified a multifunctional metabolite, TMAO, which, on the one hand, could be exploited by *Mtb* to modulate its own respiration and, on the other hand, induces deleterious effects on the host, including increased cardiovascular risk and renal insufficiency.[121,122]

Mtb Infection Dysregulates Host Immunometabolism

Innate immunity plays a key role in the pathophysiological course of pulmonary TB. Canonically, the innate response includes recognition of pathogen-associated molecular patterns (PAMPs), which induces diverse events, including inflammation, cell differentiation, and proliferation. Several findings in this study suggest that host immunometabolism is dysregulated following *Mtb* infection. For example, the following metabolic shifts (Supporting Table S4) could contribute to inflammation: (i) alterations in iNOS-related metabolites;[123] (ii) alterations in XO-related metabolites, which may contribute to IL-1β secretion through regulation of the NRLP3 inflammasome;[124] and (iii) increases in succinate levels, which has been shown to induce the release of proinflammatory cytokines through stabilization of HIF-1α.[62]

We found altered abundances of amino acids, which have been found to play a key role in immune-related processes (Supporting Table S4). For example, increased levels of several amino acids (i.e., arginine, glutamine, tryptophan) can

https://dx.doi.org/10.1021/acs.jproteome.9b00868
J. Proteome Res. 2020, 19, 2053−2070

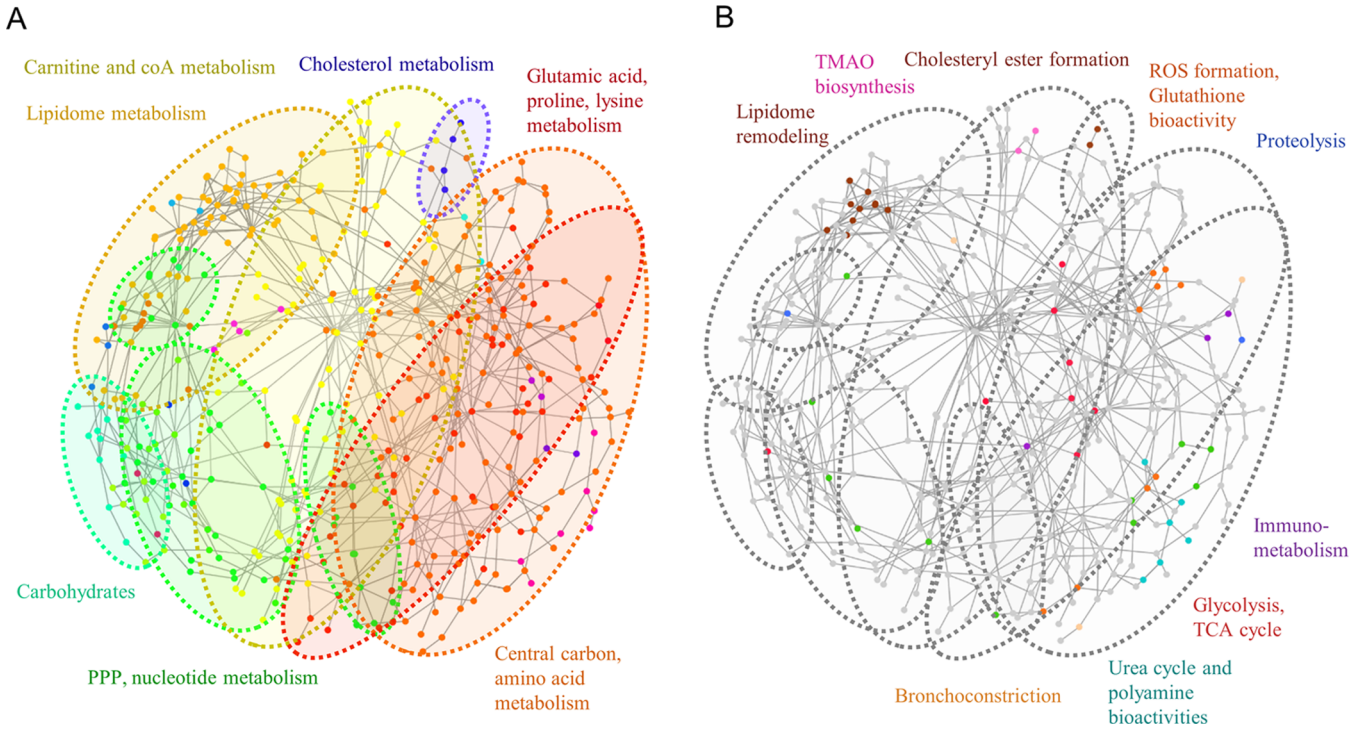

Figure 9. Metabolic subnetwork topology and network clustering analysis. (A) Color-coded map indicating the discrete clustering analysis results and major metabolite families found in clusters. (B) Superimposition of the different TB disease-associated alterations described in previous sections with the distinct network clusters.

potentially be sensed by the mechanistic target of rapamycin (mTOR) in mice, which is involved in a plethora of functions, including T-cell and monocyte differentiation and lipid synthesis.[125] Increased arginine and citrulline levels in our disease model have been related to T-cell proliferation and survival against infection.[126,127] Tryptophan and its degradation metabolites through the LPS-induced kynurenine pathway are key players in immunomodulation and immune proliferation.[128] The highly increased levels of kynurenine found in *Mtb*$^{+}$4*w* and *Mtb*$^{+}$9*w* suggest an alteration of the kynurenine pathway, which may exert deleterious effects on the immune system given that inhibition of indoleamine 2,3-dioxygenase (IDO) activity promotes control of TB infection.[129]

Subnetwork Modularity Reveals Connections between Distinct *Mtb*-Associated Pathobiological Processes

A subnetwork matrix containing the metabolites found in the study as well as bridging nodes was parsed and curated from MetaboNetworks. The resulting metabolic subnetwork was composed of 435 nodes and 739 edges. Using discrete ModuLand algorithms, we identified 21 modules. High ModuLand betweenness centrality values were assigned to metabolites including pyruvate, AMP, aspartate, serine, glutamate, glycine, glutathione, and cysteine, which were previously identified in our study as notably altered upon disease onset and progression. These results suggest that alterations in the abundances of such metabolites may have an impact on several biological processes arising from different metabolic pathways gathered in the network structure. In addition, different clusters could be observed (Figure 9A). Small clusters matched to specific pathways such as nicotinic acid metabolism and cholesterol biosynthesis. Overall, several network modules encompassed chemically similar metabolites involved in functionally described pathways. These included modules grouping carbohydrates, lipidome-related compounds, nucleotides and PPP compounds, carnitine and coA-related metabolites, glutamate and lysine-related compounds, and central carbon and amino acid metabolism. These clustering results provide evidence that clusters present in the network share a common biological role and suggest that alterations in one module are more prone to causing alterations in the modules with a higher number of intermodular edges, thereby providing a holistic view of cluster-specific metabolic alterations during TB. Overlapping of the different *Mtb*-associated biological alterations reflected in the metabolites from the previous sections (Figure 9B) reveals that, with the exception of cholesteryl esters and TMAO-related metabolites, the majority of lipidome remodeling-associated compounds conform to a tight cluster notably distant from the rest of the perturbations. In addition, metabolites related to disease-associated processes were mostly represented in the glutamate, proline, and lysine cluster or in the central carbon metabolism cluster, both being highly interconnected. These results suggest that proteolysis, and immunometabolism, alterations in the urea cycle and the polyamine metabolism are functional processes strongly related to the central carbon metabolism, which can have a joint impact via the metabolome.

CONCLUSIONS

Overall, our data emphasize that critical metabolic changes occur in the mouse lung metabolome of *Mtb*-infected mice, which are substantially altered or even reversed with disease progression, manifesting the dynamic nature of metabolic alterations. The non-targeted metabolomic approach in this study allowed the discovery of metabolic signatures of distinct pathobiological processes, several of which confirm previous observations during *Mtb* infection. Furthermore, network analysis has permitted the evaluation of comprehensive

https://dx.doi.org/10.1021/acs.jproteome.9b00868
J. Proteome Res. 2020, 19, 2053−2070

interconnections between previously and newly described TB-related metabolic processes. Also, specific metabolic alterations canonically described as inflammatory and anti-inflammatory macrophage polarization markers were found in both $Mtb^{+}4w$ and $Mtb^{+}9w$, suggesting that different macrophage polarization subpopulations may coexist in the *Mtb*-infected lung. Clustering analysis of samples revealed closer clustering of $Mtb^{+}9w$ and Mtb^{-} mice, suggesting the return of several metabolite abundances to control levels, after their alteration during the acute immune response occurring in $Mtb^{+}4w$ mice. Nonetheless, the levels of metabolites indicate highly non-compensated metabolic processes, such as proteolysis and macronutrient consumption, which are likely to reflect disease progression and worsening in $Mtb^{+}9w$. Importantly, to the best of our knowledge, this is the first report indicating that high abundances of TMAO found in the TB lung may be linked to a negative impact on the host and a possible positive impact on *Mtb*.

To contextualize the vast amount of general data generated in this study, consensus OPLS-DA has allowed data fusion and significance assessment in a technique-independent manner, providing a high-throughput-oriented statistical test for determining alterations in the metabolome. Both cOPLS-DA and SUS plots highlighted the importance of performing multiplatform studies in our model, given the specific metabolic coverage and group separation achieved by each MS-based metabolomic platform. Hence, cOPLS-DA models could be used to determine altered metabolic pathways in both ORA and PA and highlight possible altered metabolic pathways. Given the notable consistency between cOPLS-DA VIP values and percentages of change, both parameters could be used to interpret manually the alterations in specific pathways not detected by metabolite representation algorithms. Collectively, these advances allowed us to accurately contextualize and interpret metabolic changes triggered by *Mtb*, which was not previously possible.

Finally, in this study, new and previously described metabolic alterations arising from pathological processes that were modulated by TB disease were integrated into a network model that demonstrated the collective interdependent metabolic modulations induced with TB disease progression. This will contribute to our understanding of the progression of *Mtb* pathogenesis and potentially serve as a foundation for new host-directed therapeutic strategies.

■ ASSOCIATED CONTENT

Supporting Information

The Supporting Information is available free of charge at https://pubs.acs.org/doi/10.1021/acs.jproteome.9b00868.

Curated data matrix representing qualitative and quantitative parameters of the entire metabolomics data set, along with information on metabolic feature characteristics, annotations, normalized abundances per sample, cOPLS-DA variable importance in the projection and SUS plot correlation loading values (detailed legend provided in an additional spreadsheet found in the file) (XLSX)

Qualitative and quantitative NAD^{+} properties in CE-TOF/MS analysis of uninfected and *Mtb*-infected mice (XLSX)

Overrepresentation analysis and pathway analysis results showing the associated *p*-value for the altered metabolic pathways in each specific group comparison (XLSX)

Data matrix containing percentage of change and VIP values for each specific metabolite present in the experimental data and mentioned in the manuscript, sorted by the Results and Discussion subsection (XLSX)

Metabolic clustering analysis of the entire metabolomics data set showing the differences in normalized abundances of metabolites from uninfected (Mtb^{-}), and 4 ($Mtb^{+}4w$) and 9 ($Mtb^{+}9w$) weeks postinfection mice (PDF)

Pulmonary TB metabolic subnetwork following the .sif format indicating the connectivity between different enzymatic reactions, including the different metabolites annotated in the resource (TXT)

■ AUTHOR INFORMATION

Corresponding Author

Coral Barbas − *Centro de Metabolómica y Bioanálisis (CEMBIO), Facultad de Farmacia, Universidad San Pablo-CEU, CEU Universities, Boadilla del Monte 28660, Spain;* orcid.org/0000-0003-4722-491X; Phone: 913724700; Email: cbarbas@ceu.es

Authors

Miguel Fernández-García − *Centro de Metabolómica y Bioanálisis (CEMBIO), Facultad de Farmacia, Universidad San Pablo-CEU, CEU Universities, Boadilla del Monte 28660, Spain;* orcid.org/0000-0003-4114-0766

Fernanda Rey-Stolle − *Centro de Metabolómica y Bioanálisis (CEMBIO), Facultad de Farmacia, Universidad San Pablo-CEU, CEU Universities, Boadilla del Monte 28660, Spain*

Julien Boccard − *School of Pharmaceutical Sciences, University of Lausanne and University of Geneva, Geneva 1211, Switzerland*

Vineel P. Reddy − *Department of Microbiology, University of Alabama at Birmingham, Birmingham, Alabama 35294, United States*

Antonia García − *Centro de Metabolómica y Bioanálisis (CEMBIO), Facultad de Farmacia, Universidad San Pablo-CEU, CEU Universities, Boadilla del Monte 28660, Spain*

Bridgette M. Cumming − *Africa Health Research Institute, Durban 4001, South Africa*

Adrie J. C. Steyn − *Department of Microbiology and UAB Centers for AIDS Research and Free Radical Biology, University of Alabama at Birmingham, Birmingham, Alabama 35294, United States; Africa Health Research Institute, Durban 4001, South Africa;* orcid.org/0000-0001-9177-8827

Serge Rudaz − *School of Pharmaceutical Sciences, University of Lausanne and University of Geneva, Geneva 1211, Switzerland*

Complete contact information is available at: https://pubs.acs.org/10.1021/acs.jproteome.9b00868

Author Contributions

M.F.-G. and F.R.-S. contributed equally to this work. J. B. and S. R. contributed with statistical aspects related to the multiblock data analysis. V.P.R. contributed with the animal model. M.F.-G., F.R.-S, A.G., and C.B. (CEMBIO) contributed with the multiplatform metabolomics formal analysis and data processing. All the authors contributed to the discussion of results and writing. All authors have given approval to the final version of the manuscript.

Notes

The authors declare no competing financial interest.

https://dx.doi.org/10.1021/acs.jproteome.9b00868
J. Proteome Res. 2020, 19, 2053−2070

The mass spectrometry data have been deposited to the Metabolomics Workbench Data Repository (https://www.metabolomicsworkbench.org/) via the NIH Data Repository with the data set identifier ST001328.

■ ACKNOWLEDGMENTS

The co-authors would like to acknowledge funding from the Spanish Ministry of Economy and Competitiveness (RTI2018-095166-B-I00). M.F-G. acknowledges Fundación Universitaria San Pablo CEU for his Ph.D. fellowship. This work was supported by NIH grants R01Al111940, R61AI138280, R01AI137043 and the Bill and Melinda Gates Foundation award OPP1130017 (AJCS). The research was also co-funded by the South African Medical Research Council (AJCS). We acknowledge Joanna Godzien, Estanislao Nistal Villán and Francisco Javier Rupérez Pascualena (San Pablo CEU University) for useful discussions and their valuable contributions. Figure 1B and the TOC graphic were created with BioRender.

■ REFERENCES

(1) Centers for Disease Control and Prevention. The Difference Between Latent TB Infection and TB Disease. https://www.cdc.gov/tb/publications/factsheets/general/ltbiandactivetb.html (accessed March 21, 2018).

(2) World Health Organization. *Global Tuberculosis Report*; 2017. https://www.who.int/tb/publications/global_report/gtbr2017_main_text.pdf.

(3) Dheda, K.; Gumbo, T.; Maartens, G.; Dooley, K. E.; McNerney, R.; Murray, M.; Furin, J.; Nardell, E. A.; London, L.; Lessem, E.; Theron, G.; van Helden, P.; Niemann, S.; Merker, M.; Dowdy, D.; Van Rie, A.; Siu, G. K.; Pasipanodya, J. G.; Rodrigues, C.; Clark, T. G.; Sirgel, F. A.; Esmail, A.; Lin, H. H.; Atre, S. R.; Schaaf, H. S.; Chang, K. C.; Lange, C.; Nahid, P.; Udwadia, Z. F.; Horsburgh, C. R.; Churchyard, G. J.; Menzies, D.; Hesseling, A. C.; Nuermberger, E.; McIlleron, H.; Fennelly, K. P.; Goemaere, E.; Jaramillo, E.; Low, M.; Jara, C. M.; Padayatchi, N.; Warren, R. M. The epidemiology, pathogenesis, transmission, diagnosis, and management of multidrug-resistant, extensively drug-resistant, and incurable tuberculosis. *Lancet Respir. Med.* **2017**, *5*, 291−360.

(4) du Preez, I.; Luies, L.; Loots, D. T. The application of metabolomics toward pulmonary tuberculosis research. *Tuberculosis* **2019**, *115*, 126−139.

(5) Fernández-García, M.; Rojo, D.; Rey-Stolle, F.; García, A.; Barbas, C. Metabolomic-Based Methods in Diagnosis and Monitoring Infection Progression. In *Metabolic Interaction in Infection*, 1st ed.;Silvestre, R.; Torrado, E., Eds.; Springer: 2018; pp 283−315.

(6) Mirsaeidi, M.; Banoei, M. M.; Winston, B. W.; Schraufnagel, D. E. Metabolomics: Applications and Promise in Mycobacterial Disease. *Ann. Am. Thorac. Soc.* **2015**, *12*, 1278−1287.

(7) Rhee, K. Y.; de Carvalho, L. P.; Bryk, R.; Ehrt, S.; Marrero, J.; Park, S. W.; Schnappinger, D.; Venugopal, A.; Nathan, C. Central carbon metabolism in *Mycobacterium tuberculosis*: an unexpected frontier. *Trends Microbiol.* **2011**, *19*, 307−314.

(8) Beste, D. J.; Nöh, K.; Niedenführ, S.; Mendum, T. A.; Hawkins, N. D.; Ward, J. L.; Beale, M. H.; Wiechert, W.; McFadden, J. 13C-flux spectral analysis of host-pathogen metabolism reveals a mixed diet for intracellular *Mycobacterium tuberculosis*. *Chem. Biol.* **2013**, *20*, 1012−1021.

(9) Singh, A.; Crossman, D. K.; Mai, D.; Guidry, L.; Voskuil, M. I.; Renfrow, M. B.; Steyn, A. J. *Mycobacterium tuberculosis* WhiB3 maintains redox homeostasis by regulating virulence lipid anabolism to modulate macrophage response. *PLoS Pathog.* **2009**, *5*, No. e1000545.

(10) Cumming, B. M.; Addicott, K. W.; Adamson, J. H.; Steyn, A. J. *Mycobacterium tuberculosis* induces decelerated bioenergetic metabolism in human macrophages. *eLife* **2018**, *7*, No. e39169.

(11) Reddy, V. P.; Chinta, K. C.; Saini, V.; Glasgow, J. N.; Hull, T. D.; Traylor, A.; Rey-Stolle, F.; Soares, M. P.; Madansein, R.; Rahman, M. A.; Barbas, C.; Nargan, K.; Naidoo, T.; Ramdial, P. K.; George, J. F.; Agarwal, A.; Steyn, A. J. C. Ferritin H Deficiency in Myeloid Compartments Dysregulates Host Energy Metabolism and Increases Susceptibility to *Mycobacterium tuberculosis* infection. *Front. Immunol.* **2018**, *9*, No. 860.

(12) Gleeson, L. E.; Sheedy, F. J.; Palsson-McDermott, E. M.; Triglia, D.; O'Leary, S. M.; O'Sullivan, M. P.; O'Neill, L. A.; Keane, J. Cutting Edge: *Mycobacterium tuberculosis* Induces Aerobic Glycolysis in Human Alveolar Macrophages That Is Required for Control of Intracellular Bacillary Replication. *J. Immunol.* **2016**, *196*, 2444−2449.

(13) Braverman, J.; Stanley, S. A. Nitric Oxide Modulates Macrophage Responses to *Mycobacterium tuberculosis* Infection through Activation of HIF-1 α and repression of NF-κB. *J. Immunol.* **2017**, *199*, 1805−1816.

(14) Qualls, J. E.; Murray, P. J. Immunometabolism within the tuberculosis granuloma: amino acids, hypoxia, and cellular respiration. *Semin. Immunopathol.* **2016**, *38*, 139−152.

(15) Weiner, J.; Maertzdorf, J.; Sutherland, J. S.; Duffy, F. J.; Thompson, E.; Suliman, S.; McEwen, G.; Thiel, B.; Parida, S. K.; Zyla, J.; Hanekom, W. A.; Mohney, R. P.; Boom, W. H.; Mayanja-Kizza, H.; Howe, R.; Dockrell, H. M.; Ottenhoff, T. H. M.; Scriba, T. J.; Zak, D. E.; Walzl, G.; Kaufmann, S. H. E. The GC6-74 consortium. Metabolite changes in blood predict the onset of tuberculosis. *Nat. Commun.* **2018**, *9*, No. 5208.

(16) Shin, J. H.; Yang, J. Y.; Jeon, B. Y.; Yoon, Y. J.; Cho, S. N.; Kang, Y. H.; Ryu, D. H.; Hwang, G. S. 1H NMR-based metabolomic profiling in mice infected with *Mycobacterium tuberculosis*. *J. Proteome Res.* **2011**, *10*, 2238−2247.

(17) Somashekar, B. S.; Amin, A. G.; Rithner, C. D.; Troudt, J.; Basaraba, R.; Izzo, A.; Crick, D. C.; Chatterjee, D. Metabolic profiling of lung granuloma in *Mycobacterium tuberculosis* infected guinea pigs: ex vivo 1H magic angle spinning NMR studies. *J. Proteome Res.* **2011**, *10*, 4186−4195.

(18) Somashekar, B. S.; Amin, A. G.; Tripathi, P.; MacKinnon, N.; Rithner, C. D.; Shanley, C. A.; Basaraba, R.; Henao-Tamayo, M.; Kato-Maeda, M.; Ramamoorthy, A.; Orme, I. M.; Ordway, D. J.; Chatterjee, D. Metabolomic signatures in guinea pigs infected with epidemic-associated W-Beijing strains of *Mycobacterium tuberculosis*. *J. Proteome Res.* **2012**, *11*, 4873−4884.

(19) Emwas, A.-H. M. The strengths and weaknesses of NMR spectroscopy and mass spectrometry with particular focus on metabolomics research. *Methods Mol. Biol.* **2015**, *1277*, 161−193.

(20) Naz, S.; García, A.; Barbas, C. Multiplatform analytical methodology for metabolic fingerprinting of lung tissue. *Anal. Chem.* **2013**, *85*, 10941−10948.

(21) Guijas, C.; Montenegro-Burke, J. R.; Domingo-Almenara, X.; Palermo, A.; Warth, B.; Hermann, G.; Koellensperger, G.; Huan, T.; Uritboonthai, W.; Aisporna, A. E.; Wolan, D. W.; Spilker, M. E.; Benton, H. P.; Siuzdak, G. METLIN: A Technology Platform for Identifying Knowns and Unknowns. *Anal. Chem.* **2018**, *90*, 3156−3164.

(22) Fiehn, O. Metabolite profiling in Arabidopsis. In *Arabidopsis Protocols*, 2nd ed.; Salinas, J.; Sanchez-Serrano, J. J., Eds.; Springer: Berlin, 2006; pp 439−447.

(23) Kind, T.; Wohlgemuth, G.; Lee, D. Y.; Lu, Y.; Palazoglu, M.; Shahbaz, S.; Fiehn, O. FiehnLib: mass spectral and retention index libraries for metabolomics based on quadrupole and time-of-flight gas chromatography/mass spectrometry. *Anal. Chem.* **2009**, *81*, 10038−10048.

(24) Gil de la Fuente, A.; Godzien, J.; Fernández López, M.; Rupérez, F. J.; Barbas, C.; Otero, A. Knowledge-based metabolite annotation tool: CEU Mass Mediator. *J. Pharm. Biomed. Anal.* **2018**, *154*, 138−149.

(25) Brockman, S. A.; Roden, E. V.; Hegeman, A. D. Van Krevelen diagram visualization of high resolution-mass spectrometry metabolomics data with OpenVanKrevelen. *Metabolomics* **2018**, *14*, No. 48.

(26) Godzien, J.; Alonso-Herranz, V.; Barbas, C.; Grace Armitage, E. Controlling the quality of metabolomics data: new strategies to get the best out of the QC sample. *Metabolomics* **2015**, *11*, 518−528.

https://dx.doi.org/10.1021/acs.jproteome.9b00868
J. Proteome Res. 2020, 19, 2053−2070

(27) Boccard, J.; Rutledge, D. N. A consensus orthogonal partial least squares discriminant analysis (OPLS-DA) strategy for multiblock Omics data fusion. *Anal. Chim. Acta* **2013**, *769*, 30−39.
(28) Chong, J.; Soufan, O.; Li, C.; Caraus, I.; Li, S.; Bourque, G.; Wishart, D. S.; Xia, J. MetaboAnalyst 4.0: towards more transparent and integrative metabolomics analysis. *Nucleic Acids Res.* **2018**, *46*, W486−W494.
(29) Kanehisa, M.; Furumichi, M.; Tanabe, M.; Sato, Y.; Morishima, K. KEGG: new perspectives on genomes, pathways, diseases and drugs. *Nucleic Acids Res.* **2017**, *45*, D353−D361.
(30) Posma, J. M.; Robinette, S. L.; Holmes, E.; Nicholson, J. K. MetaboNetworks, an interactive Matlab-based toolbox for creating, customizing and exploring sub-networks from KEGG. *Bioinformatics* **2014**, *30*, 893−895.
(31) Szalay-Beko, M.; Palotai, R.; Szappanos, B.; Kovács, I. A.; Papp, B.; Csermely, P. ModuLand plug-in for Cytoscape: determination of hierarchical layers of overlapping network modules and community centrality. *Bioinformatics* **2012**, *28*, 2202−2204.
(32) Shannon, P.; Markiel, A.; Ozier, O.; Baliga, N. S.; Wang, J. T.; Ramage, D.; Amin, N.; Schwikowski, B.; Ideker, T. Cytoscape: a software environment for integrated models of biomolecular interaction networks. *Genome Res.* **2003**, *13*, 2498−2504.
(33) Kovács, I. A.; Palotai, R.; Szalay, M. S.; Csermely, P. Community landscapes: an integrative approach to determine overlapping network module hierarchy, identify key nodes and predict network dynamics. *PLoS One* **2010**, *5*, No. e12528.
(34) Stek, C.; Allwood, B.; Walker, N. F.; Wilkinson, R. J.; Lynen, L.; Meintjes, G. The Immune Mechanisms of Lung Parenchymal Damage in Tuberculosis and the Role of Host-Directed Therapy. *Front. Microbiol.* **2018**, *9*, No. 2603.
(35) Lugo-Villarino, G.; Hudrisier, D.; Benard, A.; Neyrolles, O. Emerging trends in the formation and function of tuberculosis granulomas. *Front. Immunol.* **2012**, *3*, No. 405.
(36) Marakalala, M. J.; Raju, R. M.; Sharma, K.; Zhang, Y. J.; Eugenin, E. A.; Prideaux, B.; Daudelin, I. B.; Chen, P. Y.; Booty, M. G.; Kim, J. H.; Eum, S. Y.; Via, L. E.; Behar, S. M.; Barry, C. E.; Mann, M.; Dartois, V.; Rubin, E. J. Inflammatory signaling in human tuberculosis granulomas is spatially organized. *Nat. Med.* **2016**, *22*, 531−538.
(37) Liu, X.; Locasale, J. W. Metabolomics: A Primer. *Trends Biochem. Sci.* **2017**, *42*, 274−284.
(38) Holmes, E.; Wilson, I. D.; Nicholson, J. K. Metabolic phenotyping in health and disease. *Cell* **2008**, *134*, 714−717.
(39) Aranibar, N.; Vassallo, J. D.; Rathmacher, J.; Stryker, S.; Zhang, Y.; Dai, J.; Janovitz, E. B.; Robertson, D.; Reily, M.; Lowe-Krentz, L.; Lehman-McKeeman, L. Identification of 1- and 3-methylhistidine as biomarkers of skeletal muscle toxicity by nuclear magnetic resonance-based metabolic profiling. *Anal. Biochem.* **2011**, *410*, 84−91.
(40) Sugawara, T.; Ito, Y.; Nishizawa, N.; Suzuki, H.; Kobayashi, H.; Nagasawa, T. Measurement of the rate of myofibrillar protein degradation using the arteriovenous difference in plasma 3-methylhistidine concentration of rats. *J. Nutr. Sci. Vitaminol.* **2009**, *55*, 381−384.
(41) Gupta, K. B.; Gupta, R.; Atreja, A.; Verma, M.; Vishvkarma, S. Tuberculosis and nutrition. *Lung India* **2009**, *26*, 9−16.
(42) Macallan, D. C.; McNurlan, M. A.; Kurpad, A. V.; de Souza, G.; Shetty, P. S.; Calder, A. G.; Griffin, G. E. Whole body protein metabolism in human pulmonary tuberculosis and undernutrition: evidence for anabolic block in tuberculosis. *Clin. Sci.* **1998**, *94*, 321−331.
(43) Ong, C. W.; Elkington, P. T.; Friedland, J. S. Tuberculosis, pulmonary cavitation, and matrix metalloproteinases. *Am. J. Respir. Crit. Care Med.* **2014**, *190*, 9−18.
(44) Shiryaev, S. A.; Cieplak, P.; Aleshin, A. E.; Sun, Q.; Zhu, W.; Motamedchaboki, K.; Sloutsky, A.; Strongin, A. Y. Matrix metalloproteinase proteolysis of the mycobacterial HSP65 protein as a potential source of immunogenic peptides in human tuberculosis. *FEBS J.* **2011**, *278*, 3277−3286.
(45) Lindskog, C.; Fagerberg, L.; Hallström, B.; Edlund, K.; Hellwig, B.; Rahnenführer, J.; Kampf, C.; Uhlén, M.; Pontén, F.; Micke, P. The lung-specific proteome defined by integration of transcriptomics and antibody-based profiling. *FASEB J.* **2014**, *28*, 5184−5196.
(46) Toshima, M.; Ohtani, Y.; Ohtani, O. Three-dimensional architecture of elastin and collagen fiber networks in the human and rat lung. *Arch. Histol. Cytol.* **2004**, *67*, 31−40.
(47) Kim, C.; Ko, Y.; Kim, S. H.; Yoo, H. J.; Lee, J. S.; Rhee, C. K.; Lee, J. H.; Kim, T. H.; Lim, S. Y.; Yoo, K. H.; Seo, J. B.; Oh, Y. M.; Lee, S. D.; Park, Y. B.; Lee, J.-H. Urinary desmosine is associated with emphysema severity and frequent exacerbation in patients with COPD. *Respirology* **2018**, *23*, 176−181.
(48) Seddon, J.; Kasprowicz, V.; Walker, N. F.; Yuen, H. M.; Sunpath, H.; Tezera, L.; Meintjes, G.; Wilkinson, R. J.; Bishai, W. R.; Friedland, J. S.; Elkington, P. T. Procollagen III N-terminal propeptide and desmosine are released by matrix destruction in pulmonary tuberculosis. *J. Infect. Dis.* **2013**, *208*, 1571−1579.
(49) Taooka, Y.; Maeda, A.; Hiyama, K.; Ishioka, S.; Yamakido, M. Effects of neutrophil elastase inhibitor on bleomycin-induced pulmonary fibrosis in mice. *Am. J. Respir. Crit. Care Med.* **1997**, *156*, 260−265.
(50) Toyoki, Y.; Sasaki, M.; Narumi, S.; Yoshihara, S.; Morita, T.; Konn, M. Semiquantitative evaluation of hepatic fibrosis by measuring tissue hydroxyproline. *Hepatogastroenterology* **1998**, *45*, 2261−2264.
(51) Hothersall, J. S.; Gordge, M.; Noronha-Dutra, A. A. Inhibition of NADPH supply by 6-aminonicotinamide: effect on glutathione, nitric oxide and superoxide in J774 cells. *FEBS Lett.* **1998**, *434*, 97−100.
(52) Shi, L.; Salamon, H.; Eugenin, E. A.; Pine, R.; Cooper, A.; Gennaro, M. L. Infection with *Mycobacterium tuberculosis* induces the Warburg effect in mouse lungs. *Sci. Rep.* **2016**, *5*, No. 18176.
(53) Williams, N. C.; O'Neill, L. A. J. A Role for the Krebs Cycle Intermediate Citrate in Metabolic Reprogramming in Innate Immunity and Inflammation. *Front. Immunol.* **2018**, *9*, No. 141.
(54) Jha, A. K.; Huang, S. C.; Sergushichev, A.; Lampropoulou, V.; Ivanova, Y.; Loginicheva, E.; Chmielewski, K.; Stewart, K. M.; Ashall, J.; Everts, B.; Pearce, E. J.; Driggers, E. M.; Artyomov, M. N. Network integration of parallel metabolic and transcriptional data reveals metabolic modules that regulate macrophage polarization. *Immunity* **2015**, *42*, 419−430.
(55) Michelucci, A.; Cordes, T.; Ghelfi, J.; Pailot, A.; Reiling, N.; Goldmann, O.; Binz, T.; Wegner, A.; Tallam, A.; Rausell, A.; Buttini, M.; Linster, C. L.; Medina, E.; Balling, R.; Hiller, K. Immune-responsive gene 1 protein links metabolism to immunity by catalyzing itaconic acid production. *Proc. Natl. Acad. Sci. U.S.A.* **2013**, *110*, 7820−7825.
(56) Strelko, C. L.; Lu, W.; Dufort, F. J.; Seyfried, T. N.; Chiles, T. C.; Rabinowitz, J. D.; Roberts, M. F. Itaconic acid is a mammalian metabolite induced during macrophage activation. *J. Am. Chem. Soc.* **2011**, *133*, 16386−16389.
(57) Tallam, A.; Perumal, T. M.; Antony, P. M.; Jäger, C.; Fritz, J. V.; Vallar, L.; Balling, R.; Del Sol, A.; Michelucci, A. Gene Regulatory Network Inference of Immunoresponsive Gene 1 (IRG1) Identifies Interferon Regulatory Factor 1 (IRF1) as Its Transcriptional Regulator in Mammalian Macrophages. *PLoS One* **2016**, *11*, No. e0149050.
(58) Lampropoulou, V.; Sergushichev, A.; Bambouskova, M.; Nair, S.; Vincent, E. E.; Loginicheva, E.; Cervantes-Barragan, L.; Ma, X.; Huang, S. C.; Griss, T.; Weinheimer, C. J.; Khader, S.; Randolph, G. J.; Pearce, E. J.; Jones, R. G.; Diwan, A.; Diamond, M. S.; Artyomov, M. N. Itaconate Links Inhibition of Succinate Dehydrogenase with Macrophage Metabolic Remodeling and Regulation of Inflammation. *Cell Metab.* **2016**, *24*, 158−166.
(59) Krátký, M.; Vinšová, J. Advances in mycobacterial isocitrate lyase targeting and inhibitors. *Curr. Med. Chem.* **2012**, *19*, 6126−6137.
(60) Pham, T. V.; Murkin, A. S.; Moynihan, M. M.; Harris, L.; Tyler, P. C.; Shetty, N.; Sacchettini, J. C.; Huang, H. L.; Meek, T. D. Mechanism-based inactivator of isocitrate lyases 1 and 2 from *Mycobacterium tuberculosis*. *Proc. Natl. Acad. Sci. U.S.A.* **2017**, *114*, 7617−7622.
(61) Nair, S.; Huynh, J. P.; Lampropoulou, V.; Loginicheva, E.; Esaulova, E.; Gounder, A. P.; Boon, A. C. M.; Schwarzkopf, E. A.; Bradstreet, T. R.; Edelson, B. T.; Artyomov, M. N.; Stallings, C. L.; Diamond, M. S. Irg1 expression in myeloid cells prevents

https://dx.doi.org/10.1021/acs.jproteome.9b00868
J. Proteome Res. 2020, 19, 2053−2070

immunopathology during M. tuberculosis infection. *J. Exp. Med.* **2018**, *215*, 1035−1045.
(62) Tannahill, G. M.; Curtis, A. M.; Adamik, J.; Palsson-McDermott, E. M.; McGettrick, A. F.; Goel, G.; Frezza, C.; Bernard, N. J.; Kelly, B.; Foley, N. H.; Zheng, L.; Gardet, A.; Tong, Z.; Jany, S. S.; Corr, S. C.; Haneklaus, M.; Caffrey, B. E.; Pierce, K.; Walmsley, S.; Beasley, F. C.; Cummins, E.; Nizet, V.; Whyte, M.; Taylor, C. T.; Lin, H.; Masters, S. L.; Gottlieb, E.; Kelly, V. P.; Clish, C.; Auron, P. E.; Xavier, R. J.; O'Neill, L. A. Succinate is an inflammatory signal that induces IL-1β through HIF-1α. *Nature* **2013**, *496*, 238−242.
(63) O'Neill, L. A.; Kishton, R. J.; Rathmell, J. A guide to immunometabolism for immunologists. *Nat. Rev. Immunol.* **2016**, *16*, 553−565.
(64) Fahien, L. A.; Kmiotek, E. H.; MacDonald, M. J.; Fibich, B.; Mandic, M. Regulation of malate dehydrogenase activity by glutamate, citrate, alpha-ketoglutarate, and multienzyme interaction. *J. Biol. Chem.* **1988**, *263*, 10687−10697.
(65) Freire, D. M.; Gutierrez, C.; Garza-Garcia, A.; Grabowska, A. D.; Sala, A. J.; Ariyachaokun, K.; Panikova, T.; Beckham, K. S. H.; Colom, A.; Pogenberg, V.; Cianci, M.; Tuukkanen, A.; Boudehen, Y. M.; Peixoto, A.; Botella, L.; Svergun, D. I.; Schnappinger, D.; Schneider, T. R.; Genevaux, P.; de Carvalho, L. P. S.; Wilmanns, M.; Parret, A. H. A.; Neyrolles, O. An NAD+ Phosphorylase Toxin Triggers *Mycobacterium tuberculosis* Cell Death. *Mol. Cell* **2019**, *73*, 1282−1291.e8.
(66) Tak, U.; Vlach, J.; Garza-Garcia, A.; William, D.; Danilchanka, O.; de Carvalho, L. P. S.; Saad, J. S.; Niederweis, M. The tuberculosis necrotizing toxin is an NAD+ and NADP+ glycohydrolase with distinct enzymatic properties. *J. Biol. Chem.* **2018**, *294*, 3024−3026.
(67) Pajuelo, D.; Gonzalez-Juarbe, N.; Tak, U.; Sun, J.; Orihuela, C. J.; Niederweis, M. NAD+ Depletion Triggers Macrophage Necroptosis, a Cell Death Pathway Exploited by *Mycobacterium tuberculosis*. *Cell Rep.* **2018**, *24*, 429−440.
(68) Gopinathan, K. P.; Sirsi, M.; Vaidyanathan, C. S. Nicotinamide-Adenine Dinucleotide-Glycohydrolase Activity in Experimental Tuberculosis. *Biochem. J.* **1965**, *94*, 446−451.
(69) Yu, X. H.; Zhang, D. W.; Zheng, X. L.; Tang, C. K. Itaconate: an emerging determinant of inflammation in activated macrophages. *Immunol. Cell Biol.* **2019**, *97*, 134−141.
(70) Tan, H. Y.; Wang, N.; Li, S.; Hong, M.; Wang, X.; Feng, Y. The Reactive Oxygen Species in Macrophage Polarization: Reflecting Its Dual Role in Progression and Treatment of Human Diseases. *Oxid. Med. Cell. Longevity* **2016**, *2016*, No. 2795090.
(71) Jamaati, H.; Mortaz, E.; Pajouhi, Z.; Folkerts, G.; Movassaghi, M.; Moloudizargari, M.; Adcock, I. M.; Garssen, J. Nitric Oxide in the Pathogenesis and Treatment of Tuberculosis. *Front. Microbiol.* **2017**, *8*, No. 2008.
(72) Duque-Correa, M. A.; Kühl, A. A.; Rodriguez, P. C.; Zedler, U.; Schommer-Leitner, S.; Rao, M.; Weiner, J.; Hurwitz, R.; Qualls, J. E.; Kosmiadi, G. A.; Murray, P. J.; Kaufmann, S. H.; Reece, S. T. Macrophage arginase-1 controls bacterial growth and pathology in hypoxic tuberculosis granulomas. *Proc. Natl. Acad. Sci. U.S.A.* **2014**, *111*, E4024−E4032.
(73) Liu, W.; Peng, Y.; Yin, Y.; Zhou, Z.; Zhou, W.; Dai, Y. The involvement of NADPH oxidase-mediated ROS in cytokine secretion from macrophages induced by *Mycobacterium tuberculosis* ESAT-6. *Inflammation* **2014**, *37*, 880−892.
(74) Granger, D. N.; Kvietys, P. R. Reperfusion injury and reactive oxygen species: The evolution of a concept. *Redox Biol.* **2015**, *6*, 524−551.
(75) Cao, R.; Teskey, G.; Islamoglu, H.; Abrahem, R.; Munjal, S.; Gyurjian, K.; Zhong, L.; Venketaraman, V. Characterizing the Effects of Glutathione as an Immunoadjuvant in the Treatment of Tuberculosis. *Antimicrob. Agents Chemother.* **2018**, *62*, No. e01132-18.
(76) Venketaraman, V.; Dayaram, Y. K.; Amin, A. G.; Ngo, R.; Green, R. M.; Talaue, M. T.; Mann, J.; Connell, N. D. Role of glutathione in macrophage control of mycobacteria. *Infect. Immun.* **2003**, *71*, 1864−1871.
(77) Thornalley, P. J. The glyoxalase system in health and disease. *Mol. Aspects Med.* **1993**, *14*, 287−371.
(78) Edagwa, B.; Wang, Y.; Narayanasamy, P. Synthesis of azide derivative and discovery of glyoxalase pathway inhibitor against pathogenic bacteria. *Bioorg. Med. Chem. Lett.* **2013**, *23*, 6138−6140.
(79) Richard-Greenblatt, M.; Bach, H.; Adamson, J.; Peña-Diaz, S.; Li, W.; Steyn, A. J.; Av-Gay, Y. Regulation of Ergothioneine Biosynthesis and Its Effect on *Mycobacterium tuberculosis* Growth and Infectivity. *J. Biol. Chem.* **2015**, *290*, 23064−23076.
(80) Saini, V.; Cumming, B. M.; Guidry, L.; Lamprecht, D. A.; Adamson, J. H.; Reddy, V. P.; Chinta, K. C.; Mazorodze, J. H.; Glasgow, J. N.; Richard-Greenblatt, M.; Gomez-Velasco, A.; Bach, H.; Av-Gay, Y.; Eoh, H.; Rhee, K.; Steyn, A. J. C. Ergothioneine Maintains Redox and Bioenergetic Homeostasis Essential for Drug Susceptibility and Virulence of *Mycobacterium tuberculosis*. *Cell Rep.* **2016**, *14*, 572−585.
(81) Hardbower, D. M.; Asim, M.; Luis, P. B.; Singh, K.; Barry, D. P.; Yang, C.; Steeves, M. A.; Cleveland, J. L.; Schneider, C.; Piazuelo, M. B.; Gobert, A. P.; Wilson, K. T. Ornithine decarboxylase regulates M1 macrophage activation and mucosal inflammation via histone modifications. *Proc. Natl. Acad. Sci. U.S.A.* **2017**, *114*, E751−E760.
(82) Gobert, A. P.; Wilson, K. T. Editorial: Orchestration of macrophage polarization by polyamines. *J. Leukocyte Biol.* **2012**, *91*, 677−679.
(83) Pegg, A. E. Functions of Polyamines in Mammals. *J. Biol. Chem.* **2016**, *291*, 14904−14912.
(84) Hayes, C. S.; Shicora, A. C.; Keough, M. P.; Snook, A. E.; Burns, M. R.; Gilmour, S. K. Polyamine-blocking therapy reverses immunosuppression in the tumor microenvironment. *Cancer Immunol. Res.* **2014**, *2*, 274−285.
(85) Jain, A.; Tyagi, A. K. Role of polyamines in the synthesis of RNA in mycobacteria. *Mol. Cell. Biochem.* **1987**, *78*, 3−8.
(86) Sarathy, J. P.; Lee, E.; Dartois, V. Polyamines inhibit porin-mediated fluoroquinolone uptake in mycobacteria. *PLoS One* **2013**, *8*, No. e65806.
(87) Mandal, A.; Mandal, S.; Park, M. H. Global quantitative proteomics reveal up-regulation of endoplasmic reticulum stress response proteins upon depletion of eIF5A in HeLa cells. *Sci. Rep.* **2016**, *6*, No. 25795.
(88) Melis, N.; Rubera, I.; Cougnon, M.; Giraud, S.; Mograbi, B.; Belaid, A.; Pisani, D. F.; Huber, S. M.; Lacas-Gervais, S.; Fragaki, K.; Blondeau, N.; Vigne, P.; Frelin, C.; Hauet, T.; Duranton, C.; Tauc, M. Targeting eIF5A Hypusination Prevents Anoxic Cell Death through Mitochondrial Silencing and Improves Kidney Transplant Outcome. *J. Am. Soc. Nephrol.* **2017**, *28*, 811−822.
(89) Nishimura, K.; Murozumi, K.; Shirahata, A.; Park, M. H.; Kashiwagi, K.; Igarashi, K. Independent roles of eIF5A and polyamines in cell proliferation. *Biochem. J.* **2005**, *385*, 779−785.
(90) Fessler, M. B.; Summer, R. S. Surfactant Lipids at the Host-Environment Interface. Metabolic Sensors, Suppressors, and Effectors of Inflammatory Lung Disease. *Am. J. Respir. Cell Mol. Biol.* **2016**, *54*, 624−635.
(91) Lee, W.; VanderVen, B. C.; Fahey, R. J.; Russell, D. G. Intracellular *Mycobacterium tuberculosis* exploits host-derived fatty acids to limit metabolic stress. *J. Biol. Chem.* **2013**, *288*, 6788−6800.
(92) Singh, G.; Singh, G.; Jadeja, D.; Kaur, J. Lipid hydrolizing enzymes in virulence: *Mycobacterium tuberculosis* as a model system. *Crit. Rev. Microbiol.* **2010**, *36*, 259−269.
(93) Schneider, B. E.; Behrends, J.; Hagens, K.; Harmel, N.; Shayman, J. A.; Schaible, U. E. Lysosomal phospholipase A2: a novel player in host immunity to *Mycobacterium tuberculosis*. *Eur. J. Immunol.* **2014**, *44*, 2394−2404.
(94) Honda, A.; Yamashita, K.; Ikegami, T.; Hara, T.; Miyazaki, T.; Hirayama, T.; Numazawa, M.; Matsuzaki, Y. Highly sensitive quantification of serum malonate, a possible marker for de novo lipogenesis, by LC-ESI-MS/MS. *J. Lipid Res.* **2009**, *50*, 2124−2130.
(95) Ecker, J.; Liebisch, G.; Englmaier, M.; Grandl, M.; Robenek, H.; Schmitz, G. Induction of fatty acid synthesis is a key requirement for phagocytic differentiation of human monocytes. *Proc. Natl. Acad. Sci. U.S.A.* **2010**, *107*, 7817−7822.
(96) Moon, J. S.; Lee, S.; Park, M. A.; Siempos, I. I.; Haslip, M.; Lee, P. J.; Yun, M.; Kim, C. K.; Howrylak, J.; Ryter, S. W.; Nakahira, K.; Choi,

https://dx.doi.org/10.1021/acs.jproteome.9b00868
J. Proteome Res. 2020, 19, 2053−2070

A. M. UCP2-induced fatty acid synthase promotes NLRP3 inflammasome activation during sepsis. *J. Clin. Invest.* **2015**, *125*, 665−680.
(97) Kol, S.; Kehat, I.; Adashi, E. Y. Ovarian interleukin-1-induced gene expression: privileged genes threshold theory. *Med. Hypotheses* **2002**, *58*, 6−8.
(98) Gaber, T.; Strehl, C.; Buttgereit, F. Metabolic regulation of inflammation. *Nat. Rev. Rheumatol.* **2017**, *13*, 267−279.
(99) Huang, Z.; Luo, Q.; Guo, Y.; Chen, J.; Xiong, G.; Peng, Y.; Ye, J.; Li, J. *Mycobacterium tuberculosis*-Induced Polarization of Human Macrophage Orchestrates the Formation and Development of Tuberculous Granulomas In Vitro. *PLoS One* **2015**, *10*, No. e0129744.
(100) Knight, M.; Braverman, J.; Asfaha, K.; Gronert, K.; Stanley, S. Lipid droplet formation in *Mycobacterium tuberculosis* infected macrophages requires IFN-γ/HIF-1α signaling and supports host defense. *PLoS Pathog.* **2018**, *14*, No. e1006874.
(101) Khor, V. K.; Ahrends, R.; Lin, Y.; Shen, W. J.; Adams, C. M.; Roseman, A. N.; Cortez, Y.; Teruel, M. N.; Azhar, S.; Kraemer, F. B. The proteome of cholesteryl-ester-enriched versus triacylglycerol-enriched lipid droplets. *PLoS One* **2014**, *9*, No. e105047.
(102) Cáceres, N.; Tapia, G.; Ojanguren, I.; Altare, F.; Gil, O.; Pinto, S.; Vilaplana, C.; Cardona, P. J. Evolution of foamy macrophages in the pulmonary granulomas of experimental tuberculosis models. *Tuberculosis* **2009**, *89*, 175−182.
(103) Ghosh, S.; Zhao, B.; Bie, J.; Song, J. Macrophage cholesteryl ester mobilization and atherosclerosis. *Vascul. Pharmacol.* **2010**, *52*, 1−10.
(104) Hla, T.; Dannenberg, A. J. Sphingolipid signaling in metabolic disorders. *Cell Metab.* **2012**, *16*, 420−434.
(105) Malik, Z. A.; Thompson, C. R.; Hashimi, S.; Porter, B.; Iyer, S. S.; Kusner, D. J. Cutting edge: *Mycobacterium tuberculosis* blocks Ca2+ signaling and phagosome maturation in human macrophages via specific inhibition of sphingosine kinase. *J. Immunol.* **2003**, *170*, 2811−2815.
(106) Sharma, L.; Prakash, H. Sphingolipids Are Dual Specific Drug Targets for the Management of Pulmonary Infections: Perspective. *Front. Immunol.* **2017**, *8*, No. 378.
(107) Vass, G.; Horváth, I. Adenosine and adenosine receptors in the pathomechanism and treatment of respiratory diseases. *Curr. Med. Chem.* **2008**, *15*, 917−922.
(108) Afrasiabian, S.; Mohsenpour, B.; Bagheri, K. H.; Sigari, N.; Aftabi, K. Diagnostic value of serum adenosine deaminase level in pulmonary tuberculosis. *J. Res. Med. Sci.* **2013**, *18*, 252−254.
(109) Volonté, C.; D'Ambrosi, N. Membrane compartments and purinergic signalling: the purinome, a complex interplay among ligands, degrading enzymes, receptors and transporters. *FEBS J.* **2009**, *276*, 318−329.
(110) Chan, J.; Xing, Y.; Magliozzo, R. S.; Bloom, B. R. Killing of virulent *Mycobacterium tuberculosis* by reactive nitrogen intermediates produced by activated murine macrophages. *J. Exp. Med.* **1992**, *175*, 1111−1122.
(111) MacMicking, J. D.; North, R. J.; LaCourse, R.; Mudgett, J. S.; Shah, S. K.; Nathan, C. F. Identification of nitric oxide synthase as a protective locus against tuberculosis. *Proc. Natl. Acad. Sci. U.S.A.* **1997**, *94*, 5243−5248.
(112) Kummer, W.; Wiegand, S.; Akinci, S.; Schinkel, A. H.; Wess, J.; Koepsell, H.; Haberberger, R. V.; Lips, K. S. Role of acetylcholine and muscarinic receptors in serotonin-induced bronchoconstriction in the mouse. *J. Mol. Neurosci.* **2006**, *30*, 67−68.
(113) Barfod, K. K.; Vrankx, K.; Mirsepasi-Lauridsen, H. C.; Hansen, J. S.; Hougaard, K. S.; Larsen, S. T.; Ouwenhand, A. C.; Krogfelt, K. A. The Murine Lung Microbiome Changes During Lung Inflammation and Intranasal Vancomycin Treatment. *Open Microbiol. J.* **2015**, *9*, 167−179.
(114) Clavel, T.; Lagkouvardos, I.; Blaut, M.; Stecher, B. The mouse gut microbiome revisited: From complex diversity to model ecosystems. *Int. J. Med. Microbiol.* **2016**, *306*, 316−327.
(115) Fennema, D.; Phillips, I. R.; Shephard, E. A. Trimethylamine and Trimethylamine N-Oxide, a Flavin-Containing Monooxygenase 3 (FMO3)-Mediated Host-Microbiome Metabolic Axis Implicated in Health and Disease. *Drug Metab. Dispos.* **2016**, *44*, 1839−1850.
(116) Al-Waiz, M.; Mikov, M.; Mitchell, S. C.; Smith, R. L. The exogenous origin of trimethylamine in the mouse. *Metabolism* **1992**, *41*, 135−136.
(117) Barrett, E. L.; Kwan, H. S. Bacterial reduction of trimethylamine oxide. *Annu. Rev. Microbiol.* **1985**, *39*, 131−149.
(118) Seldin, M. M.; Meng, Y.; Qi, H.; Zhu, W.; Wang, Z.; Hazen, S. L.; Lusis, A. J.; Shih, D. M. Trimethylamine N-Oxide Promotes Vascular Inflammation Through Signaling of Mitogen-Activated Protein Kinase and Nuclear Factor-κB. *J. Am. Heart Assoc.* **2016**, *5*, No. e002767.
(119) Ierardi, E.; Sorrentino, C.; Principi, M.; Giorgio, F.; Losurdo, G.; Di Leo, A. Intestinal microbial metabolism of phosphatidylcholine: a novel insight in the cardiovascular risk scenario. *Hepatobiliary Surg. Nutr.* **2015**, *4*, 289−292.
(120) Wang, Z.; Klipfell, E.; Bennett, B. J.; Koeth, R.; Levison, B. S.; Dugar, B.; Feldstein, A. E.; Britt, E. B.; Fu, X.; Chung, Y. M.; Wu, Y.; Schauer, P.; Smith, J. D.; Allayee, H.; Tang, W. H.; DiDonato, J. A.; Lusis, A. J.; Hazen, S. L. Gut flora metabolism of phosphatidylcholine promotes cardiovascular disease. *Nature* **2011**, *472*, 57−63.
(121) Kaysen, G. A.; Johansen, K. L.; Chertow, G. M.; Dalrymple, L. S.; Kornak, J.; Grimes, B.; Dwyer, T.; Chassy, A. W.; Fiehn, O. Associations of Trimethylamine N-Oxide With Nutritional and Inflammatory Biomarkers and Cardiovascular Outcomes in Patients New to Dialysis. *J. Ren. Nutr.* **2015**, *25*, 351−356.
(122) Tang, W. H. W.; Wang, Z.; Kennedy, D. J.; Wu, Y.; Buffa, J. A.; Agatisa-Boyle, B.; Li, X. S.; Levison, B. S.; Hazen, S. L. Gut microbiota-dependent trimethylamine N-oxide (TMAO) pathway contributes to both development of renal insufficiency and mortality risk in chronic kidney disease. *Circ. Res.* **2015**, *116*, 448−455.
(123) Teng, X.; Zhang, H.; Snead, C.; Catravas, J. D. Molecular mechanisms of iNOS induction by IL-1 beta and IFN-gamma in rat aortic smooth muscle cells. *Am. J. Physiol.: Cell Physiol.* **2002**, *282*, C144−52.
(124) Ives, A.; Nomura, J.; Martinon, F.; Roger, T.; LeRoy, D.; Miner, J. N.; Simon, G.; Busso, N.; So, A. Xanthine oxidoreductase regulates macrophage IL1β secretion upon NLRP3 inflammasome activation. *Nat. Commun.* **2015**, *6*, No. 6555.
(125) Weichhart, T.; Hengstschläger, M.; Linke, M. Regulation of innate immune cell function by mTOR. *Nat. Rev. Immunol.* **2015**, *15*, 599−614.
(126) Geiger, R.; Rieckmann, J. C.; Wolf, T.; Basso, C.; Feng, Y.; Fuhrer, T.; Kogadeeva, M.; Picotti, P.; Meissner, F.; Mann, M.; Zamboni, N.; Sallusto, F.; Lanzavecchia, A. L-Arginine Modulates T Cell Metabolism and Enhances Survival and Anti-tumor Activity. *Cell* **2016**, *167*, 829−842.e13.
(127) Lange, S. M.; McKell, M. C.; Schmidt, S. M.; Hossfeld, A. P.; Chaturvedi, V.; Kinder, J. M.; McAlees, J. W.; Lewkowich, I. P.; Way, S. S.; Turner, J.; Qualls, J. E. L-Citrulline Metabolism in Mice Augments CD4+ T Cell Proliferation and Cytokine Production In Vitro, and Accumulation in the Mycobacteria-infected lung. *Front. Immunol.* **2017**, *8*, No. 1561.
(128) Routy, J. P.; Routy, B.; Graziani, G. M.; Mehraj, V. The Kynurenine Pathway Is a Double-Edged Sword in Immune-Privileged Sites and in Cancer: Implications for Immunotherapy. *Int. J. Tryptophan Res.* **2016**, *9*, 67−77.
(129) Gautam, U. S.; Foreman, T. W.; Bucsan, A. N.; Veatch, A. V.; Alvarez, X.; Adekambi, T.; Golden, N. A.; Gentry, K. M.; Doyle-Meyers, L. A.; Russell-Lodrigue, K. E.; Didier, P. J.; Blanchard, J. L.; Kousoulas, K. G.; Lackner, A. A.; Kalman, D.; Rengarajan, J.; Khader, S. A.; Kaushal, D.; Mehra, S. In vivo inhibition of tryptophan catabolism reorganizes the tuberculoma and augments immune-mediated control of *Mycobacterium tuberculosis*. *Proc. Natl. Acad. Sci. U.S.A.* **2018**, *115*, E62−E71.

https://dx.doi.org/10.1021/acs.jproteome.9b00868
J. Proteome Res. 2020, 19, 2053−2070